frontiers | Frontiers in Batteries and Electrochemistry

TYPE Original Research
PUBLISHED 20 February 2024
DOI 10.3389/fbael.2024.1330604

OPEN ACCESS

EDITED BY
Chunmei Ban,
University of Colorado Boulder, United States

REVIEWED BY
Guy Marlair,
French National Institute for Industrial Environment and Risks (INERIS), France
Ben Pei,
Binghamton University, United States

*CORRESPONDENCE
Jennifer M. Pringle,
jenny.pringle@deakin.edu.au

RECEIVED 31 October 2023
ACCEPTED 25 January 2024
PUBLISHED 20 February 2024

CITATION
Sourjah A, Kang CSM, Ferrero Vallana FM, Hutt OE, O'Dell LA and Pringle JM (2024), Investigation of the benefits of the oxazolidinium cation for plastic crystal and ionic liquid electrolytes.
Front. Batteries Electrochem. 3:1330604.
doi: 10.3389/fbael.2024.1330604

Investigation of the benefits of the oxazolidinium cation for plastic crystal and ionic liquid electrolytes

Azra Sourjah[1], Colin S. M. Kang[1], Federico M. Ferrero Vallana[1], Oliver E. Hutt[2], Luke A. O'Dell[3] and Jennifer M. Pringle[1]*

[1]Institute for Frontier Materials, Deakin University, Burwood, VIC, Australia, [2]Boron Molecular, Melbourne, VIC, Australia, [3]Institute for Frontier Materials, Deakin University, Geelong, VIC, Australia

Organic ionic plastic crystals (OIPCs) are promising for developing safer energy storage electrolytes. However, there remains a significant knowledge gap regarding how different cation-anion combinations influence their core properties, and cyclic ether-based cations have received limited attention. This study reports the synthesis and characterization of OIPCs based on the *N*-ethyl-*N*-methyl-oxazolidinium cation $[C_2moxa]^+$ and demonstrates the first instance of oxazolidinium OIPCs being combined with lithium salts to create electrolytes. The $[C_2moxa]^+$ cation was paired with $[FSI]^-$, $[TFSI]^-$, $[BF_4]^-$, $[PF_6]^-$ and $[FTFSI]^-$ anions. A study of the thermal, transport and electrochemical properties was performed. Among the new salts developed, $[C_2moxa][BF_4]$ exhibited the most promising characteristics, including the lowest entropy of melting (ΔS = 7 J mol^{-1} K^{-1}), an extended phase I range (10°C–130°C), the highest conductivity of 8 x 10^{-6} S cm^{-1} at 30°C, and an electrochemical stability window of 4.8 V. When the $[C_2moxa][BF_4]$ and $[C_2moxa][FSI]$ were mixed with lithium salts (10, 20 and 50 mol% Li^+) of the same anion, the highest conductivity of 2 x 10^{-3} S cm^{-1} at 30°C was found for the 20 mol% LiFSI/$[C_2moxa][FSI]$ electrolyte. Finally, preliminary lithium plating/stripping experiments and coulombic efficiency (CE) measurements demonstrate stability for lithium cycling for all four $[C_2moxa]^+$ electrolytes.

KEYWORDS

organic ionic plastic crystals, ionic liquids, electrolytes, oxazolidinium, OIPCs

1 Introduction

The commercialization of secondary batteries across various sectors has underscored the necessity for innovative electrolyte systems that can enhance both performance and safety. While conventional liquid electrolytes have found widespread use in batteries, their compatibility with Li metal anodes remains restricted due to concerns about safety arising from dendrite growth (Fan et al., 2018). The proliferation of these dendrites can cause short circuits, thus elevating the risks of battery malfunction and potential fires. Beyond challenges related to dendrites, lithium metal batteries encounter problems like unstable interfaces and air instability limiting their practical use. The instability at the interface is linked to the formation of an unstable solid electrolyte interphase (SEI), causing issues such as higher interfacial impedance, and reduced coulombic efficiency. Hatzell et al. (2020), Han et al. (2021) Considering these challenges, engineering novel electrolyte systems that offer

enhanced safety characteristics becomes paramount for the advancement of next-generation batteries and their applications. Among the emerging options, ionic liquids (ILs) and organic ionic plastic crystals (OIPCs) have gained prominence as advanced electrolytes due to their intrinsic safety attributes, including advantageous properties such as reduced flammability (with high flash point when measurable), Diallo et al. (2013), Eshetu et al. (2017) very low vapour pressure (up to the decomposition temperature) and good thermal stability (Smiglak et al., 2006) compared to conventional organic solvents used in electrolytes, and good electrochemical stability. Scrosati et al. (2011), Wang and Xia (2011), Zhu et al. (2019).

ILs are composed solely of cations and anions and are typically liquid at room temperature (RT). Plechkova and Seddon (2008) On the other hand OIPCs are similar to ILs but exist as disordered solids at room temperature. Although OIPCs exhibit long-range order, they also show short-range disorder due to the rotational and translational motion of the ions, which imparts inherent plasticity. Jin et al. (2012) OIPCs also undergo one or more solid-solid phase transitions before melting. The intrinsic disorder in OIPCs allows good ionic conductivity, making them suitable as solid-state electrolytes. Their soft mechanical properties can also promote good contact between the electrolyte and electrode interface, during volume expansion. Macfarlane and Forsyth (2001), Tian et al. (2019) Both ILs and OIPCs offer the ability to tune their chemical and physical properties by selecting specific types of cations and anions. However, despite significant progress in OIPC development in recent years, there is still a lack of understanding regarding how different cation and anion combinations affect their properties, including thermal, ion dynamics, ionic conductivity, and electrochemical properties. Increasing the range of well-characterized OIPCs is key to addressing this knowledge gap.

The families of OIPCs developed to date are less diverse than those of ILs. Furthermore, despite the introduction of numerous novel OIPCs, their potential as battery electrolytes through the incorporation of Li^+ or Na^+ salts has been much less explored. Mixing OIPCs with lithium/sodium salts enhances the ionic conductivity of the overall electrolyte, enabling efficient ion movement (Iranipour et al., 2017). Previous studies on OIPCs as electrolytes have primarily explored organic cations, including pyrrolidinium (Forsyth et al., 2014; Yamada et al., 2019; Al-Masri et al., 2020a), ammonium (Zhou and Matsumoto, 2007; Yang et al., 2018; Yunis et al., 2020a), phosphonium (Jin et al., 2014; Makhlooghiazad et al., 2017) and guanidinium (Biernacka et al., 2020; Biernacka et al., 2021). Also, dications like 1,2-bis(*N*-ethylpyrrolidinium) ethane (Abeysooriya et al., 2022), and imidazolium (1,2-bis [*N*-(*N*'-alkylimidazolium)]ethane) (Lee et al., 2017) have been used to form OIPC electrolytes. The aforementioned cations are combined with delocalised anions such as bis(fluorosulfonyl)imide $[FSI]^-$, bis(trifluoromethanesulfonyl)imide $[TFSI]^-$, (trifluoromethane) fluorosulfonylimide $[FTFSI]^-$, tetrafluoroborate $[BF_4]^-$ and hexafluorophosphate $[PF_6]^-$. The latter, spherical anions ($[BF_4]^-$ and $[PF_6]^-$) (Yunis et al., 2019) can exhibit significant rotational disorder, while the $[FSI]^-$ and $[TFSI]^-$ species can also display conformational isomerism (cis and trans) (Jin et al., 2017). Recent OIPC research has also investigated new anions utilising the cyano group such as cyanate $[OCN]^-$ (Janikowski et al., 2011), tricyanomethanide $[TCM]^-$ (Yamaguchi et al., 2019), and fluorinated anions like 1,1,2,2,2-pentafluoro-*N*-[(1,1,2,2,2,-pentafluoroethyl)sulfonyl]imide $[BETA]^-$, 1,1,2,2,3,3-hexafluoro-*N*-[(1,1,2,2,3,3-hexafluoropropane-1,3-disulfoneimide $[CFSA]^-$ and nonafluorobutanesulfonate $[NFS]^-$ (Yamaguchi et al., 2019). However, although the properties of the neat OIPCs has been documented, the potential for these new anions in electrolyte development remains less explored.

Prior work has highlighted the significant impact that functional groups can have on the physicochemical properties of ILs, with particular attention given to the ether group (Hu and Song, 2017). The alkoxy group in the side chain offers flexibility to the cation, increasing conformational freedom, reducing viscosity, and enhancing ionic conductivity of the IL (Zhou et al., 2005; Fang et al., 2009; Navarra et al., 2017). Moreover, when cations incorporate an ether oxygen in the side chain, it can suppress IL crystallization, especially at sub-zero temperatures, further improving conductivity (Ferrari et al., 2009; Appetecchi et al., 2011). Additionally the oxygen moiety in the side chain can enhance lithium ion transport by coordinating with lithium ions and promote its dissociation from the anion (Martin et al., 2018; Shimizu et al., 2020). In other words, an ether oxygen atom can act as a Lewis base (as the ether group is an electron donor), which can solvate target ions (Li^+/Na^+) to improve the solubility of the lithium/sodium salts, ultimately increasing the ionic conductivity of the electrolyte and enhancing battery performance (Hu and Song, 2017; Navarra et al., 2017). Thus, the utilization of ether functional groups in the cationic side chain structure offers proven benefits.

While numerous studies have focused on the incorporation of ether functionality in the side chain of cationic structures, relatively few studies have explored the potential of small cyclic ether cations, (e.g., oxazolidinium, morpholinium) especially for OIPCs. For instance, in 2004, Kim et al. reported the use of *N*-ethyl-*N*-methylmorpholinium $[C_2mmor]^+$ and *N*-butyl-*N*-methylmorpholinium $[C_4mmor]^+$ cations paired with the $[TFSI]^-$ anion (Kim et al., 2004). The $[C_2mmor][TFSI]$ exhibited a melting point of 29.2°C, with three solid solid-solid phase transitions, and is thus an OIPC, while $[C_4mmor][TFSI]$ was reported to be an IL. These materials were thermally stable up to nearly 400°C, with similar electrochemical windows of 4.5 V (−2.5 V–2 V) (Choi et al., 2005). In addition, in 2010 Lane et al. reported a comprehensive study on the IL, $[C_4mmor][FSI]$ by comparing it with the piperidinium analogues (Lane et al., 2010). The addition of lithium salt to this IL increased the electrochemical stability of $[C_4mmor][FSI]$, allowing the salt to be used as an electrolyte within a Li symmetrical cell. Moreover, recently Kang et al. reported the synthesis and characterisation of *N,N*-dimethyloxazolidinium $[C_1moxa]^+$ cation, paired with anions, to examine the influence of cyclic ether on the physical and transport properties of the neat materials (Kang et al., 2021). The author also synthesised *N*-ethyl-*N*-methyloxazolidinium $[C_2moxa][FSI]$ salt, which displayed around three times higher ionic conductivity than its pyrrolidinium counterpart *N*-ethyl-*N*-methyl pyrrolidinium $[C_2mpyr][FSI]$ (5.7×10^{-6} S cm^{-1} vs 2×10^{-6} S cm^{-1} respectively, at 30°C) and had the largest free volume of the salts studied, making these $[C_2moxa]^+$ cations interesting for further study.

In this paper we present the synthesis and detailed characterisation of a range of new salts utilising the $[C_2moxa]^+$ cation paired with $[FSI]^-$, $[TFSI]^-$, $[BF_4]^-$, $[PF_6]^-$ and $[FTFSI]^-$ anions (Figure 1). The synthesis was conducted via a halide free approach

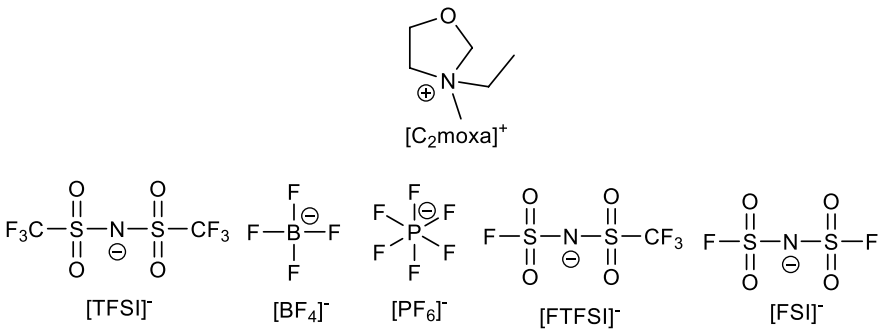

FIGURE 1
Structure and abbreviations of the cation and anions used in this study. Cation abbreviation is *N*-ethyl-*N*-methyl oxazolidinium $[C_2moxa]^+$. Anion abbreviations are bis(trifluoromethanesulfonyl)imide $[TFSI]^-$, tetrafluoroborate $[BF_4]^-$ hexafluorophosphate $[PF_6]^-$, trifluoromethanesulfonyl (fluorosulfonyl)imide $[FTFSI]^-$ and bis(fluorosulfonyl)imide $[FSI]^-$.

(via the tosylate salt intermediate) (Kang et al., 2022) aiming to mitigate the impact of halide impurities on electrochemical stability (Passerini and Appetecchi, 2013). The thermal and transport properties of all salts were investigated. Solid-state NMR analysis was used to investigate the temperature dependent ion dynamics. Cyclic voltammetry was performed to investigate the electrochemical potential window of the salts. For the first time, oxazolidinium OIPCs have been mixed with lithium salts to investigate their promise as electrolytes, for future application in batteries.

2 Experimental

2.1 Materials and methods

N-methyloxazolidine (≥97%, Boron Molecular), *N*-ethyl-*N*-methylbenzenesulfonate (≥98%, Boron molecular), lithium bis(trifluoromethanesulfonyl)imide (LiTFSI) (≥98%, Solvionic), lithium bisfluorosulfonylimide (LiFSI) (≥97%, Solvionic) lithium tetrafluoroborate ($LiBF_4$) (≥98%, Sigma Aldrich), potassium hexafluorophosphate (KPF_6) (≥98%, Sigma Aldrich) were dried at 50°C for at least 24 h before use. Anhydrous acetonitrile (MeCN) (≥99.9%, Sigma Aldrich), dichloromethane (DCM) (HPLC grade, lab supply), silver nitrate ($AgNO_3$) (LR, Chem-Supply, Australia), silver trifluoromethanesulfonate (AgOTf) (≥98%, Sigma Aldrich) and aluminium oxide (Al_2O_3) (ultra dry, 99%, Sigma Aldrich), activated charcoal (Sigma Aldrich) were used without further purification.

2.2 Purity analysis

Liquid-state ^1H (400 MHz), ^{19}F (375 MHz), ^{11}B (128 MHz) and ^{31}P (162 MHz) NMR spectra were measured on a Bruker Avance III instrument using deuterated dimethylsulfoxide (d_6-DMSO) as the solvent. For all OIPCs and IL, no impurity peaks were observed in the NMR spectra. Mass spectroscopy was performed on an Agilent 1,200 series HPLC system. For all solid salts, elemental analysis was performed at Monash University, Clayton, Australia.

Lithium was quantified using an inductively coupled plasma-mass spectrometer (ICP-MS; NexION 350X, PerkinElmer, USA). Internal standards Sc (200 ppb) and Rh (20 ppb) in 1% aqua regia were used to correct the matrix effects. The internal standard solution was mixed prior to the nebuliser using a T-piece in a 1: 1 ratio. Calibration standards for lithium and potassium (PerkinElmer, lithium, or potassium standard 1,000 ppm in 2% HNO_3) were prepared 0.1, 1, 10, 50, 100, and 500 ppb with 2% suprapur HNO_3 in each. The mass spectrometer was operated in kinetic energy discrimination mode (KED) with 50 ms dwell times, 20 sweeps, one reading and three replicates. The plasma source conditions were nebuliser gas flow 1.02 L min^{-1}, auxiliary gas flow 1.2 L min^{-1}, plasma gas flow 15 L min^{-1} and ICP RF power 1500 W. Data analysis was carried out using Syngistix (PerkinElmer) software. Signal responses were normalised to the scandium internal standard.

2.3 Differential scanning calorimetry (DSC)

The thermal analysis was carried out using a Netzsch DSC 214 Polyma with a scan rate of 10°C min^{-1} for both the heating and cooling cycles. Sample preparation was performed in an Ar-filled glove box, using a sample size of 5–10 mg in an aluminium pan. The heat flow and temperature were calibrated using cyclohexane before the measurement. The temperature range used depended upon the melting temperature of the sample (T_m), e.g., from −100°C up to 100 or 150°C. The DSC data shown were extracted from the second heating scan to eliminate the thermal history effects and provide an accurate representation of the sample's thermal behaviour. There was no significant difference observed between the first, second and third heating cycles.

2.4 Thermogravimetric analysis (TGA)

A TA-Q50 instrument system was used to perform TGA over a temperature range of 25°C–600°C. Samples weighing 5–10 mg were rapidly loaded into a platinum pan and then inserted into a stream of N_2 gas flowing at a rate of 40 mL min^{-1}. The measurements were conducted under N_2 with a heating rate of 10°C min^{-1}. The thermal

decomposition temperature was identified as the temperature at which each material lost 5% of its weight. Future studies incorporate carrying out TGA in semi oxidative atmospheres for the developed oxazolidinium electrolytes.

2.5 Electrochemical impedance spectroscopy (EIS)

Ionic conductivity measurements were carried out using Biologic MTZ 35 electrochemical impedance spectroscopy. A dip cell with platinum electrodes was used to measure conductivity within the temperature range of 30°C–100°C. The cell constant was determined by measuring 1 mM KCl solution at 30°C. The conductivity of the samples was determined by identifying the real axis intercept in the Nyquist plot of the impedance data.

2.6 Solid-state NMR linewidth measurements (static NMR)

All the ^{1}H,^{19}F and ^{13}B static NMR measurements were performed on a Bruker Avance III 300 MHz wide-bore NMR spectrometer equipped with a 5 mm HF/X double resonance probe. Samples were packed inside an Ar-filled glovebox in a 5 mm glass tube. ^{1}H static spectra were recorded with single pulse excitation, ^{19}F were recorded with a Hahn echo. The frequency scales are referenced to the ^{1}H NMR signal of tetramethylsilane (0 kHz) and the ^{19}F NMR signal of $CFCl_3$ (0 kHz) respectively. Results were analysed using the TopSpin and Dmfit software.

2.7 Pulse-field gradient nuclear magnetic resonance spectroscopy (PFG-STE NMR)

The diffusivities of the $[C_2moxa]^+$ cation, $[FSI]^-$ and $[BF_4]^-$ anions and Li^+ cations for the 10 and 20 mol% Li salts were determined using ^{1}H, ^{19}F and ^{7}Li pulsed-field gradient stimulated echo (PFG-STE NMR). The samples were packed into 5 mm NMR tubes inside an Ar-filled glovebox and the measurements were conducted on a 7.05 T Bruker Avance III spectrometer equipped with a Diff50 probe. The experiments were carried out at 25°C and every 10°C from 30°C to 70°C, with a minimum of 10 min equilibration time before each measurement and analysed using Topspin software. The STE pulse sequence was used with four scans at each gradient strength. The diffusion time was 25 ms, gradient duration was 1 ms, and the maximum gradient strength used was 2800 G cm^{-1}. The Stejskal–Tanner equation was applied to fit the signal attenuation profiles in TopSpin to obtain the diffusion coefficients.

2.8 Cyclic voltammetry (CV)

Lithium plating and stripping experiments were performed using a three-electrode cell consisting of a 3 mm nickel (Ni) working electrode, a coiled platinum wire counter electrode, and an AgOTf reference electrode. The AgOTf reference electrode was prepared from a 0.05 M solution of AgOTf and the ionic liquid $[C_3mpyr][FSI]$. Prior to each scan in the positive or negative direction, the Ni electrode was polished with 0.3 m alumina and water, while the Pt wire was cleaned by flame gun. The electrochemical potential window (EW) was performed with a Pt wire as the reference electrode, a coiled Pt wire as the counter electrode, and a Pt working electrode with a diameter of 3 mm. The Pt pseudo-reference electrode was calibrated using the ferrocenium ion/ferrocene (Fc^+/Fc) in each electrolyte studied. Analysis was conducted on a Biologic SP-200 potentiostat in a glovebox with an Ar atmosphere. The reductive scans were performed before the oxidative scans. Due to the presence of the oxygen atom in the oxazolidinium cation, using the Karl Fisher method was not possible as it would have led to a reaction between the OIPC and the KF reagent and compromised accuracy. To ensure complete drying and minimal water content in the samples, a 48 h vacuum drying process at 50°C was carried out.

3 Synthesis

3.1 *N*-ethyl-*N*-methyloxazolidinium *N*-methylbenzenesulfonate $[C_2moxa][Ts]$

To a solution of *N*-methyloxazolidine (10.0 g, 115 mmol) in acetone at 50°C, a solution of ethyl *p*-toluenesulfonate (23.0 g, 115 mmol) in acetone was added dropwise. After the exothermic reaction settled, the mixture was heated to reflux with stirring overnight under argon (Ar) atmosphere. After cooling to −30°C with stirring, the solid which separated was filtered off, rinsed with cold acetone, and dried at 70°C under vacuum to afford an off white solid. (24.7 g, 75%). ^{1}H NMR (200 MHz, $(CD_3)_2SO$: 1.29 ppm (t, CH_2CH_3, 3H), 3.44 ppm (s, NCH_3, 3H), 3.62 ppm (s, -$ArCH_3$, 3H), 3.66 ppm (q, NCH_2CH_3, 2H), 3.70 ppm (t, CH_2CH_2O, 2H), 4.19 ppm (t, NCH_2CH_2, 2H), 4.26 ppm (d, NCH_2O, 2H), 7.13 ppm (d, J_{HH} = 8.0 Hz, ArCH, 2H), 7.49 ppm (d, J_{HH} = 8.0Hz, ArCH, 2H).

3.2 *N*-ethyl-*N*-methyloxazolidinium bis(trifluoromethanesulfonyl)imide $[C_2moxa][TFSI]$

$[C_2moxa][Ts]$ (5.5 g, 19 mmol) was dissolved in ~30 mL of MeCN and added dropwise to a solution of LiTFSI (5.6 g, 20 mmol) and MeCN (~30 mL) cooled with an ice bath while stirring under Ar. Upon complete addition, a white precipitate formed, and the mixture was left to stir under Ar overnight. The white precipitate (by-product) was removed by filtration and the resulting filtrate was isolated and passed through an Al_2O_3 column for further purification. Activated charcoal was added to the filtrate, which was then left stirring overnight. The charcoal was removed by filtration, and the MeCN was removed under vacuum using a rotary evaporator to obtain a white solid product (3.8 g, 51%). ^{1}H NMR (200 MHz, $(CD_3)_2SO$): 1.32 ppm (t, J_{HH} = 7.4 Hz, –NCH_2CH_3, 3H), 3.34 ppm (s, NCH_3, 3H), 3.45 ppm (q, J_{HH} = 7.4 Hz, NCH_2CH_3, 2H), 3.65 ppm (t, J_{HH} 7.4 Hz, NCH_2CH_2O, 2H),

4.23 ppm (t, J_{HH} = 7.4 Hz, NCH_2CH_2O, 2H), 4.82 ppm (q, NCH_2O, 2H). ^{19}F NMR (375 MHz, $(CD_3)_2SO$): −78.71 ppm (CF_3). ES^+ m/z 116.1 $(C_6H_{14}NO)^+$, ES^- m/z 280.0 ($NS_2O_4F_2$). Anal. calculated for $C_6H_{14}N_2O_5S_2F_2$; C, 24.47; H, 3.53; N, 7.06; found: C, 24.45; H, 3.53; N, 7.05. Potassium content (ICP-MS): 50 ppm. The melting point measured manually was 50°C.

3.3 *N*-ethyl-*N*-methyloxazolidinium tetrafluoroborate [C_2moxa][BF_4]

[C_2moxa][Ts] (10.9 g, 38 mmol) was dissolved in ~30 mL of MeCN and added dropwise to a solution of $LiBF_4$ (3.6 g, 38 mmol) and MeCN (~30 mL) cooled in an ice bath while stirring under Ar. Upon complete addition, a white precipitate formed, and the mixture was left to stir under Ar. The white precipitate (by-product) was removed by filtration and the resulting filtrate was isolated and passed through an Al_2O_3 column for further purification. Activated charcoal was added to the filtrate, which was then left stirring overnight. The charcoal was removed by filtration, and the MeCN was removed under vacuum using a rotary evaporator to obtain a white hygroscopic solid (3.7 g, 48.0%). ^1H NMR (200 MHz, $(CD_3)_2SO$): 1.30 ppm (t, J_{HH} = 7.4 Hz–NCH_2CH_3, 3H), 3.30 ppm (s, NCH_3, 3H), 3.45 ppm (q, J_{HH} = 7.4 Hz, NCH_2CH_3, 2H), 3.65 ppm (t, J_{HH} 7.4 Hz, NCH_2CH_2O, 2H), 4.24 ppm (t, J_{HH}= 7.4 Hz, NCH_2CH_2O, 2H), 4.82 ppm (q, NCH_2O, 2H). ^{19}F NMR (375 MHz, $(CD_3)_2SO$): −148.25 (BF4). ^{11}B NMR (128 MHz, $(CD_3)_2SO$): −1.29 ppm (BF4). ES^+ m/z 116.1 $(C_6H_{14}NO)^+$, ES^- m/z 86.9 $(BF_{4-})^-$. Anal calculated for $C_6H_{14}NOBF_4$; C, 35.47; H, 6.89; N, 6.89; found: C, 35.35; H, 6.80; N, 6.83. Lithium content (ICP-MS): 91 ppm. The melting point measured manually was 130°C–135°C.

3.4 *N*-ethyl-*N*-methyloxazolidinium hexafluorophosphate [C_2moxa][PF_6]

[C_2moxa][Ts] (3.5 g, 20 mmol) was dissolved in ~35 mL of MeCN. The solution was added dropwise to a solution of KPF_6 (3.7 g, 20 mmol) in MeCN (~35 mL) while stirring under Ar. Upon complete addition, a white precipitate formed, and the mixture was left to stir under Ar overnight. The mixture was then filtered, and the resulting filtrate was isolated and passed through a charcoal and Al_2O_3 column for further purification. The final solution was passed through a syringe filter and MeCN was removed under vacuum using a rotary evaporator to obtain a white sticky solid. (2.8 g, 55.0%).^1H NMR (200 MHz, $(CD_3)_2SO$): 1.30 ppm (t, J_{HH} = 7.4 Hz–NCH_2CH_3, 3H), 3.37 ppm (s, NCH_3, 3H), 3.44 ppm (q, J_{HH} = 7.4 Hz, NCH_2CH_3, 2H), 3.65 ppm (t, J_{HH} 7.4 Hz, NCH_2CH_2O, 2H), 4.24 ppm (t, J_{HH}= 7.4 Hz, NCH_2CH_2O, 2H), 4.82 ppm (q, NCH_2O, 2H). ^{19}F NMR (375 MHz, $(CD_3)_2SO$): −71.0, −69.1 (F). ^{31}P,$CD_3)_2SO$: −131.02, −135.41–144.20, −148.59–152.98–157.37 ppm (P). ES^+ m/z 116.1 $(C_6H_{14}NO)^+$, ES^- m/z 144.9.9 $(PF_{6-})^-$. Anal calculated for $C_6H_{14}NOPF_6$; C, 27.57; H, 5.36; N, 5.36; found: C, 27.57; H, 5.27; N, 5.39. Potassium content (ICP-MS): 13.4 ppm. The melting point was too high to be measured manually.

3.5 *N*-ethyl-*N*-methyloxazolidinium trifluoromethanesulfonyl (fluorosulfonyl) imide [C_2moxa][FTFSI]

[C_2moxa][Ts] (4.6 g, 16 mmol) was dissolved in ~30 mL of MeCN. The solution was added dropwise to a solution of LiFTFSI (3.9 g, 16 mmol) and MeCN (~30 mL) while stirring under Ar. Upon complete addition, a white precipitate formed, and the mixture was left to stir under Ar overnight. The mixture was then filtered, and the MeCN was removed under vacuum to obtain a solid product. The solid was mixed with DCM and left in the freezer overnight. The solution was filtered through a syringe filter. Activated charcoal was added to the filtrate, which was then left to stir. The resulting mixture was filtered, and the DCM was removed under vacuum using a rotary evaporator to obtain a light-yellow liquid product (2.6 g, 46%).^1H NMR (400 MHz, $(CD_3)_2SO$): ^1H NMR (200 MHz, $(CD_3)_2SO$): 1.30 ppm (t, J_{HH} = 7.4 Hz–NCH_2CH_3, 3H), 3.30 ppm (s, NCH_3, 3H), 3.45 ppm (q, J_{HH} = 7.4 Hz, NCH_2CH_3, 2H), 3.65 ppm (t, J_{HH} 7.4 Hz, NCH_2CH_2O, 2H), 4.24 ppm (t, J_{HH}= 7.4 Hz, NCH_2CH_2O, 2H), 4.82 ppm (q, NCH_2O, 2H). ^{19}F NMR (375 MHz, $(CD_3)_2SO$): −79.85 (CF_3), 54.94 (F) ppm. ES^+ m/z 115.9 $(C_6H_{14}NO)^+$ ES^- m/z 229.7 ($NO_4S_2CF_4$). Potassium content (ICP-MS): 86 ppm.

3.6 *N*-ethyl-*N*-methyloxazolidinium bis(fluorosulfonyl)imide [C_2moxa][FSI]

[C_2moxa][Ts] (10.9 g, 38 mmol) was dissolved in ~30 mL of MeCN and added dropwise under an ice bath to a solution of LiFSI (3.6 g, 38 mmol) and MeCN (~30 mL) while stirring under Ar. Upon complete addition, a white precipitate formed, and the mixture was left to stir under Ar. The mixture was filtered out and the resulting filtrate was isolated and passed through an Al_2O_3 column for further purification, followed by addition of activated charcoal in MeCN, left stirring at RT overnight. The charcoal was filtered out, and the MeCN was removed under vacuum using a rotary evaporator to obtain a white hygroscopic solid. ^1H NMR (200 MHz, $(CD_3)_2SO$): 1.30 ppm (t, J_{HH} = 7.4 Hz–NCH_2CH_3, 3H), 3.33 ppm (s, NCH_3, 3H), 3.46 ppm (q, J_{HH} = 7.4 Hz, NCH_2CH_3, 2H), 3.65 ppm (t, J_{HH} 7.4 Hz, NCH_2CH_2O, 2H), 4.23 ppm (t, J_{HH}= 7.4 Hz, NCH_2CH_2O, 2H), 4.82 ppm (q, NCH_2O, 2H). ^{19}F NMR (375 MHz, $(CD_3)_2SO$): 53.22 ppm (F). ES^+ m/z 116.0 $(C_6H_{14}NO)$ ES^- m/z 179.9 ($NS_2O_2F_2$). Anal. calculated for $C_6H_{14}N_2O_5S_2F_2$; C, 24.29; H, 4.72; N, 9.44; found: C, 24.27; H, 4.56; N, 9.40. Potassium content (ICP-MS): 150 ppm. The melting point measured manually was 130°C–135°C.

3.7 Preparation of electrolytes

[C_2moxa][BF_4] was mixed with $LiBF_4$ (10, 20 and 50 mol %) by dissolving the required amount in MeCN and then combining. The MeCN was then removed by rotary evaporator. Subsequently the samples were dried under vacuum at 50°C for 48 h. The same procedure was also

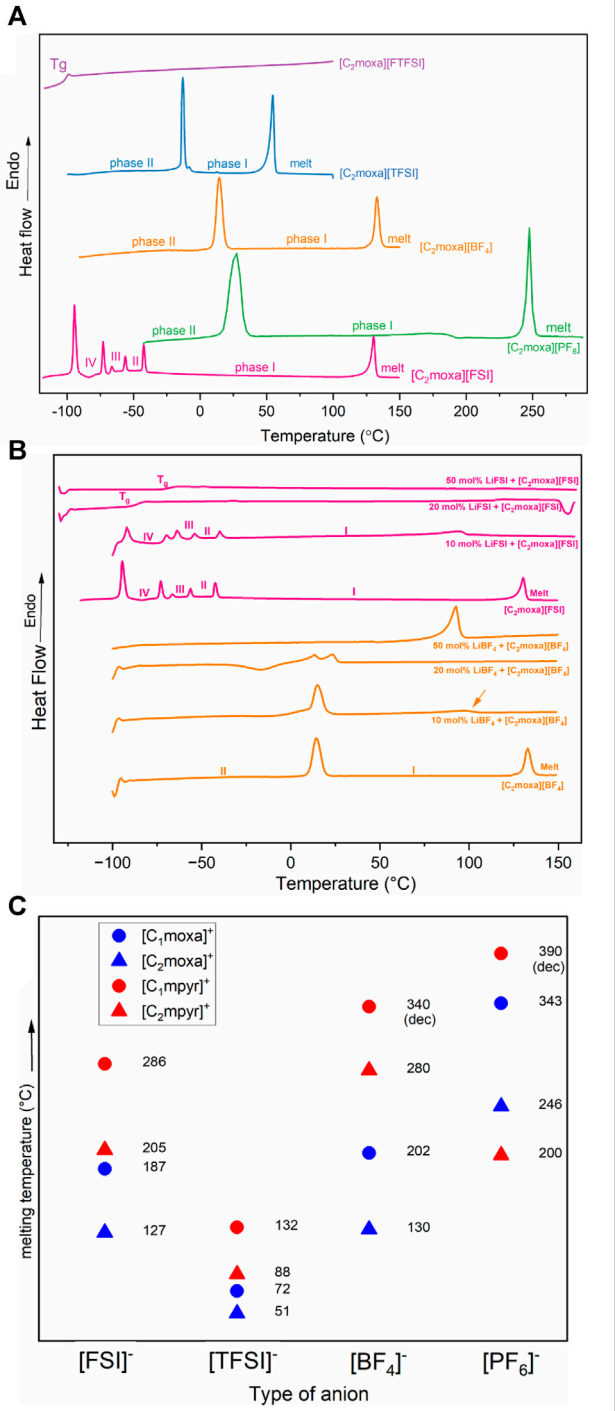

FIGURE 2
(A) DSC thermograms showing the second heating cycle for neat $[C_2moxa]^+$ −based salts. **(B)** DSC thermograms showing the second heating cycle for $[C_2moxa][BF_4]$ and $[C_2moxa][FSI]$, 10, 20 and 50 mol% electrolyte systems. All DSC traces were recorded at 10°C min^{-1} **(C)** comparison of melting points of the neat oxazolidinium and pyrrolidinium-based salts. The blue colour indicates the oxazolidinium salts ($[C_1moxa]^+$, $[C_2moxa]^+$) and red colour indicates the pyrrolidinium salts ($[C_1mpyr]^+$, $[C_2mpyr]^+$ for a clear comparison (Forsyth et al., 2001; Golding et al., 2001; Smiglak et al., 2006; Kang et al., 2021).

employed to prepare 10, 20% and 50 mol% LiFSI in $[C_2moxa][FSI]$. Selected compositions were analysed by DSC, EIS, PFG-NMR, and electrochemical testing.

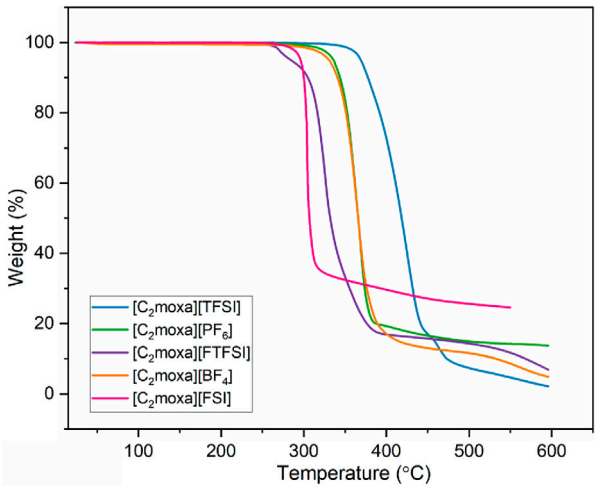

FIGURE 3
Thermogravimetric analysis of the oxazolidinium -based salts.

4 Results and discussion

4.1 Thermal properties

The thermal properties of $[C_2moxa]^+$ salts, as analysed by differential scanning calorimetry (DSC) and thermogravimetric analysis (TGA), are presented in Figure 2 and Figure 3 respectively. The transition temperatures and entropy changes of the transitions are shown in Table 1. It is evident that the thermal behaviour of these salts is strongly influenced by the type of anion present, resulting in a range of melting points spanning from below room temperature to over 100°C. By incorporating the ethyl oxazolidinium cation, a novel room temperature ionic liquid $[C_2moxa][FTFSI]$ was formed, while $[C_2moxa][TFSI]$, $[C_2moxa][BF_4]$ and $[C_2moxa][PF_6]$ salts exhibited plastic crystal behaviour.

These newly discovered OIPCs exhibit at least one solid-solid phase transition prior to melting. By convention the highest temperature solid phase is referred to as phase I, while lower temperature phases are named phase II, III, etc. (Macfarlane and Forsyth, 2001) These phases are associated with the onset of rotational and/or translational motions of the ions, signifying a transformation from an ordered crystalline phase to a highly disordered solid structure before melting (Thomas et al., 2023). Two of the materials exhibit a relatively low entropy of fusion ΔS_f (<20 J mol^{-1} K^{-1}), in accordance with Timmermans classification of plasticity for molecular plastic crystals (Timmermans, 1961). Among the studied salts, $[C_2moxa][BF_4]$ stands out with the lowest ΔS_f of 7 J mol^{-1} K^{-1}. This observation strongly suggests that the salt possesses a disordered structure in phase I. This is likely due to the fact that $[C_2moxa][BF_4]$ undergoes a large solid-solid phase II-I transition at 10°C with an entropy change of 17 J mol^{-1} K^{-1}. The phase I of this salt extends from 10°C to 130°C, which makes $[C_2moxa][BF_4]$ particularly advantageous for potential application as an electrolyte around room temperature, as phase I represents the most disordered phase of the salt.

In contrast the $[C_2moxa][TFSI]$ salt displays a phase II-I transition at −15°C, with a ΔS_{II-I} value of 18 J mol^{-1} K^{-1}. It has a

TABLE 1 Transition temperatures (T_{s-s},T_m, T_{dec} or T_g) and entropy change (ΔS) of $[C_2moxa]^+$ salts as determined by DSC.

	V-IV		IV-III		III-II		II-I		I-Melt		T_g (°C)	T_{dec} (°C)
	T_{s-s} ± 1 (°C)	ΔS ± 10% (J mol^{-1} K^{-1})	T_{s-s} ± 1 (°C)	ΔS ± 10% (J mol^{-1} K^{-1})	T_{s-s} ± 1 (°C)	ΔS ± 10% (J mol^{-1} K^{-1})	T_{s-s} ± 1 (°C)	ΔS ± 10% (J mol^{-1} K^{-1})	T_m ± 1 (°C)	ΔS_f ± 10% (J mol^{-1} K^{-1})		
$[C_2moxa][FSI]$	−96	17	−74	4	−58	2	−44	4	127	8		280
$[C_2moxa][TFSI]$							−15	18	51	22		369
$[C_2moxa][BF_4]$							10	17	130	7		331
$[C_2moxa][FTFSI]$											−103	284
$[C_2moxa][PF_6]$							18	42	246	13		336

low melting point at 51°C, accompanied by an ΔS_f of 22 J mol^{-1} K^{-1}, slightly exceeding Timmerman's criteria. Not all OIPCs meet this criterion for plasticity: in some instances, one ionic species may exhibit minimal rotational or translational motion (either the cation or anion), which becomes activated only at the melting point, resulting in a high ΔS_f value (MacFarlane et al., 2001). Notably, during the phase II-I transition of $[C_2moxa][TFSI]$, an additional small peak is observed alongside the main phase II-I transition peak (Figure 2A). To investigate this further, a subsequent scan, at a lower scan rate (2°C min^{-1}) was performed, revealing that the phase II-I transition consists of two slightly overlapping transitions (Supplementary Figure S2).

The $[C_2moxa][PF_6]$ salt stands out as having a substantial ΔS_{II-I} value of 42 J mol^{-1} K^{-1}, notably surpassing those previously reported for other $[PF_6]^-$-based OIPCs, such as diethyl (methyl) (isobutyl) phosphonium $[P_{1,2,2,i4}][PF_6]$ (ΔS_{II-I}= 4 J mol^{-1} K^{-1}) (Jin et al., 2012), *N*-isopropyl-*N*-methylpyrrolidinium $[C_{(i3)}mpyr][PF_6]$ (ΔS_{II-I}= 5 J mol^{-1} K^{-1}) (Al-Masri et al., 2020a), hexamethylguanidinium $[HMG][PF_6]$ (ΔS_{II-I}= 19 J mol^{-1} K^{-1}) (Yunis et al., 2019). This higher entropy phase II-I transition in $[C_2moxa][PF_6]$ indicates a greater degree of disorder in phase I, a characteristic that aligns with its high conductivity and disorder in the static NMR, as discussed in the upcoming section. Furthermore the $[C_2moxa][PF_6]$ salt exhibits a wide temperature range for phase I, spanning from 18°C until its melting point at 246°C.

Small and symmetrical anions like $[BF_4]^-$ and $[PF_6]^-$ generally result in higher melting points for OIPCs and ILs due to strong electrostatic interactions and efficient crystal packing between the cation and anion (Cha et al., 2005; Matsumoto et al., 2014), as seen in $[C_2moxa][PF_6]$ (T_m = 246°C). However, $[C_2moxa][BF_4]$ exhibits an unexpectedly low melting point of 130°C. Additionally, the lower melting point in $[C_2moxa][TFSI]$ (T_m = 51°C) compared to $[C_2moxa][FSI]$ (T_m = 127°C) is attributed to the larger size and increased charge delocalization of the $[TFSI]^-$ anion. Similar trends have been observed in salts containing cations like ammonium ($[N_{1111}]^+$) (Yunis et al., 2020a), phosphonium ($[P_{1222}]^+$) (Armel et al., 2011), and pyrrolidinium ($[C_2epyr]^+$, $[C_2mpyr]^+$) (Yamada et al., 2019). However, a different trend is seen in salts featuring larger cations like *N*-methyl-*N*-propylpyrrolidinium $[C_3mpyr]^+$, *N*-methyl-*N*-butylpyrrolidinium $[C_4mpyr]^+$ and tetraethylammonium $[N_{2222}]^+$, emphasizing the significance of both cation and anion characteristics in determining crystal arrangement and lattice energy (Kunze et al., 2010a; Kunze et al., 2010b).

The presence of an oxygen atom in the $[C_2moxa]^+$ cation leads to lower melting points in the studied salts compared to the pyrrolidinium analogues. For instance, $[C_2moxa][BF_4]$ has a melting point of 130°C, compared to the non-ether containing analogue $[C_2mpyr][BF_4]$ at 280°C (Forsyth et al., 2001; Iranipour et al., 2017). Similarly, $[C_2moxa][TFSI]$ exhibits a lower melting point than $[C_2mpyr][TFSI]$ (91°C vs 280°C) (Hill et al., 2002). The lower melting points observed in $[C_2moxa][BF_4]$ and $[C_2moxa][TFSI]$ compared to their non-ether containing counterparts can be attributed to the oxygen atom in the oxazolidinium cation weakening the electrostatic interaction between the cation and anion, and resulting in lower melting points due to less cationic symmetry (Matsumoto et al., 2005; Zhou et al., 2006). This phenomenon was widely observed in previous ionic liquid studies where the introduction of a short ether group(s) to the alkyl side chain of various cations resulted in decreased melting points (Matsumoto et al., 2005; Fang et al., 2011; Navarra et al., 2017). In contrast, $[C_2moxa][PF_6]$ deviates from this trend, with a slightly higher melting point of 246°C compared to $[C_2mpyr][PF_6]$ with a melting point of 200°C (Forsyth et al., 2001).

The $[FTFSI]^-$ anion combined with the $[C_2moxa]^+$ cation forms an ionic liquid with a glass transition (T_g) temperature of −103°C. Only the glass transition feature was observed, consistent with literature reports on pyrrolidinium-based $[FTFSI]^-$ salts, which also exhibit low T_g values ranging from −103 to −107°C (Reiter et al., 2013). The low melting point of $[C_2moxa][FTFSI]$ is primarily attributed to the asymmetrical nature of the $[FTFSI]^-$ anion, which likely hinders tight packing and subsequently lowers the lattice energy of the salt (Montanino et al., 2012).

The newly synthesised ethyl-substituted OIPCs, including $[C_2moxa][TFSI]$, $[C_2moxa][BF_4]$, and $[C_2moxa][PF_6]$, exhibit lower melting temperatures (T_m= 51, 130, and 246°C, respectively) than the methyl-substituted analogues $[C_1moxa]$

[TFSI], [C_1moxa][BF_4], and [C_1moxa][PF_6] (T_m= 72, 202, and 343°C, respectively) (Kang et al., 2021). This is likely a result of lower cationic symmetry, and the trend aligns with prior literature, where increasing alkyl chain length generally leads to a decrease in the melting point of OIPCs. For example, [C_1mpyr][FSI], with dimethyl substitution, has a higher melting point (T_m = 286°C) than the ethyl-substituted salt [C_2mpyr][FSI] (T_m = 205°C) (MacFarlane et al., 1999). These observations also correlate with previously reported positron annihilation spectroscopy (PALS) results, where [C_2moxa][FSI] showed a higher free volume (FFV = 977 a.u.) than [C_1moxa][FSI] (FFV = 885 a.u.), indicating less tightly packed ions. (Kang et al., 2021). Figure 2C highlights the lower melting points resulting from the introduction of an oxygen moiety in the cation (i.e., oxazolidinium vs pyrrolidinium) and also the reduction in the melting points with the extension of the alkyl chain from methyl to ethyl (C_2 vs. C_1).

Thermogravimetric analysis (TGA) is commonly used to assess the thermal stability of ILs and OIPCs (Kerner et al., 2015; Yunis et al., 2019). Both dynamic (also known as rising temperature TGA) and isothermal temperature analysis can be done to access short and long term stability respectively (Wooster et al., 2006; Eshetu et al., 2017). In this study, we investigated the effect of pairing the $[C_2moxa]^+$ cation with various anions on the decomposition temperatures of the resulting salts using dynamic TGA, defining the decomposition temperature (T_{dec}) as the temperature at which 5% weight loss occurs, with a heating rate of 10°C min^{-1} (Figure 3). The choice of a 5% mass loss serves as a reference point for the initiation of material decomposition, facilitating consistent comparison of thermal decomposition temperatures (T_d) for the examined salts (Ramesh et al., 2011; Theivaprakasam et al., 2015).

The decomposition temperatures of the [C_2moxa][BF_4], [C_2moxa][TFSI], and [C_2moxa][PF_6] salts are all above 300°C, while the [C_2moxa][FTFSI] exhibited a slightly lower decomposition temperature of 284°C. Previous literature has reported that $[FTFSI]^-$ based salts have decomposition temperatures intermediate between $[FSI]^-$ and $[TFSI]^-$ based salts (Reiter et al., 2013; Yunis et al., 2019). A plateau is observed for [C_2moxa][FTFSI] (270°C–320°C), suggesting a potential two-step decomposition of the ionic liquid. This can be due to the SO_2 evolution upon F and CF_3 release due to the instability of the S-F chemical bond compared to the S-C bond, as reported by Jeong et al. for FTFSI salts with trimethyl isobutyl ammonium cation (N_{111i4}) (Jeong et al., 2019). Among the $[C_2moxa]^+$ salts, [C_2moxa][TFSI] demonstrated the highest decomposition temperature at 369°C, surpassing that of [C_2moxa][FSI] (T_{dec} = 280°C) (Kang et al., 2021). This trend has been observed in other families of OIPCs, such as pyrrolidinium (Eshetu et al., 2017), phosphonium (Armel et al., 2011), ammonium (Jeong et al., 2019) and guanidinium (Yunis et al., 2019) where salts containing $[FSI]^-$ anions showed lower thermal stability compared to those with $[TFSI]^-$ anions. The difference in thermal stability can be attributed to the relatively weaker fluorine-sulphur bond compared to carbon-sulphur and fluorine-carbon bonds (Jeong et al., 2019). Both [C_2moxa][BF_4] and [C_2moxa][PF_6] salts exhibited similar thermal stabilities, with T_{dec} of 331°C and 336°C, respectively. A similar trend was observed when pairing $[C_1moxa]^+$ with $[PF_6]^-$ and $[BF_4]^-$ salts (343°C and 323°C, respectively) (Kang et al., 2021). While $[PF_6]^-$ and $[BF_4]^-$ based salts are known to form OIPCs that typically undergo decomposition before melting (e.g., tetramethyl ammonium [N_{1111}][BF_4](T_{dec}= 378°C), tetraethylphosphonium [P_{2222}][PF_6](T_{dec}= 333°C), [$C_{(i3)}$mpyr][BF_4] (T_{dec} = 305°C), [$C_{(i3)}$mpyr][PF_6] (T_{dec} = 305°C) (Matsumoto et al., 2014; Yunis et al., 2020b)), it is interesting to note that [C_2moxa][BF_4] and [C_2moxa][PF_6] salts melt before the decomposition occurs (Table 1). This behaviour is akin to that observed in phosphonium OIPCs [e.g., [P_{1i444}][BF_4] (T_m= 36°C, T_{dec} = 220°C), [P_{122i4}][PF_6] (T_m = 139°C, T_{dec} = 270°C)] (Armel et al., 2011). Thus, this highlights the significance of the cation-anion combination in determining the thermal behaviour of these organic salts, where both the cation and anion influence the decomposition of these OIPCs.

The oxazolidinium OIPCs synthesized in this study generally exhibit lower decomposition temperatures compared to their pyrrolidinium counterparts, except for [C_2moxa][BF_4] (T_{dec} = 331°C) which has a higher T_{dec} than [C_2mpyr][BF_4] (280°C) (Forsyth et al., 2001). Previous literature also shows that incorporating an oxygen atom into the cation leads to decreased T_{dec} values. For instance, for decomposition temperatures of the $[BF_4]^-$ and $[TFSI]^-$ series, *N*-butyl-*N*-methyloxazolidinium [C_4moxa][TFSI] (T_{dec} = 327°C)< [C_4mpyr][TFSI] (T_{dec} = 431°C), *N*-butyl-*N*-methyl morpholinium [C_4mmor][TFSI] (T_{dec} = 398°C) < *N*-butyl-*N*-methyl piperidinium [C_4mpip][TFSI] (T_{dec} = 423°C), [C_4moxa][BF_4] (T_{dec} = 322°C)< [C_4mpyr][BF_4] (T_{dec} = 403°C), [C_4mmor][BF_4](T_{dec} = 386°C)< [C_4mpip][BF_4] (T_{dec} = 403°C) (Zhou et al., 2006). Incorporation of an ether group into the alkyl side chain of ionic liquid cations also decreases thermal stability (Navarra et al., 2017). It is hypothesised that the lower thermal stability of salts with ether functional groups may be influenced by the relatively high acidity of the proton of the $-NCH_2O-$moiety that can undergo the thermal decomposition first (Zhou et al., 2006). Direct comparisons are challenging due to variations in scan rates and measurement conditions used by different research groups. Future studies incorporate carrying out TGA in semi oxidative atmospheres for the developed oxazolidinium electrolytes. Nonetheless, these oxazolidinium-based salts demonstrate sufficient thermal stability, above 250°C, making them suitable for various energy applications, such as battery electrolytes.

4.2 Transport properties

When evaluating the suitability of an OIPC as an electrolyte, one crucial factor to consider is its ionic conductivity. Solid-state electrolytes face ongoing challenges in achieving desirable transport properties (Wei et al., 2020). The conductivities of OIPCs can vary significantly based on the specific cation and anion present, which also influence the thermal properties. To enable the use of OIPCs as electrolytes in Li or Na batteries they are mixed with Li^+ or Na^+ salts, often using the same anion as the OIPC (Howlett et al., 2009), which can result in significant improvements in conductivity, often by several orders of magnitude. Here we first compare the properties of the neat salts (Figure 4A), to evaluate the impact of the cyclic ether cation and different anions on the transport properties, before investigating selected OIPC/Li salt mixtures (Figure 4B). The ionic conductivity of

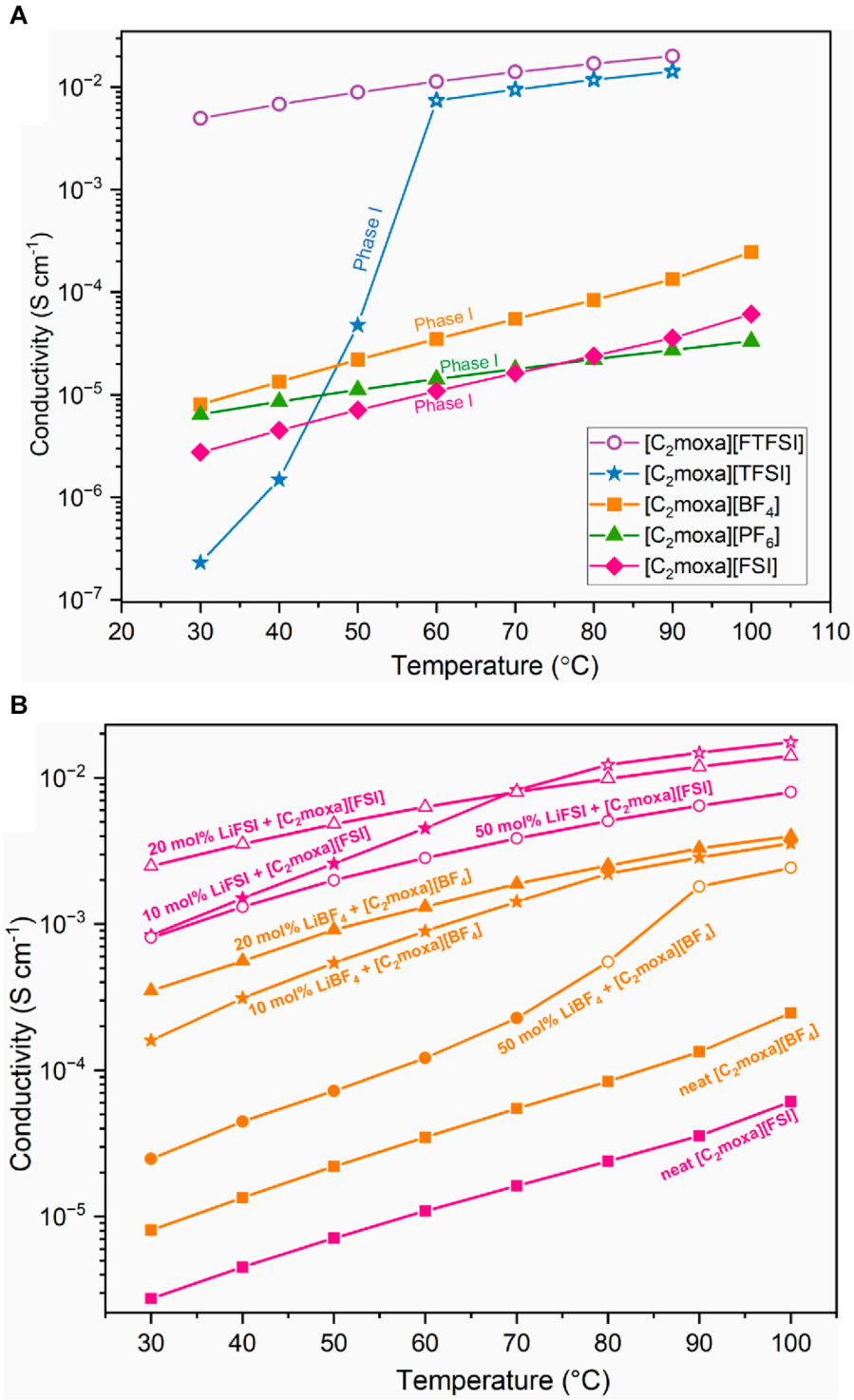

FIGURE 4
(A) Ionic conductivity of the oxazolidinium -based salts. **(B)** Ionic conductivities of the 10, 20 and 50 mol% electrolyte mixtures of [C_2moxa][BF_4] (orange) and [C_2moxa][FSI] (pink). Solid symbols indicate the quasi-solid phase and hollow symbol indicates the liquid phase. The numerical values of the ionic conductivities of above systems are included in Supplementary Table S1, S2, all of which were reproducible.

[C_2moxa]$^+$ based salts are strongly influenced by different anions. The heating and cooling curves exhibited consistent behavior across all three cycles, displaying only minor thermal hysteresis. Among the salts studied, the IL [C_2moxa][FTFSI] exhibits the highest ionic conductivity, with a value of 5×10^{-3} S cm^{-1} at 30°C (T_g = −103°C, Table 1). Previous literature reports similar conductivities for ionic liquids featuring the FTFSI anion, such as [C_3mpyr][FTFSI] (3.5×10^{-3} S cm^{-1} at 20°C, T_g = −107°C), *N*-methoxyethyl-*N*-methylpyrrolidinium [C_{201}mpyr][FTFSI] (4.5×10^{-3} S cm^{-1} at 20°C, T_g = −104°C) and *N*-butyl-*N*-methylpyrrolidinium [C_4mpyr]

[FTFSI] (4.9×10^{-3} S cm^{-1} at 20°C, T_g = −103°C) (Reiter et al., 2013). Hence, the conductivity observed for [C_2moxa][FTFSI] aligns with the trend where lower T_g values correlate with higher conductivity, consistent with existing literature.

Among the newly developed OIPCs, [C_2moxa][BF_4] demonstrates the highest conductivity, approximately 8×10^{-6} S cm^{-1} at 30°C. This aligns with its low ΔS_f value of 7 J mol^{-1} K^{-1} that reflects a more disordered phase I (as a result of the large phase II-I transition) which leads to a higher conductivity. Comparatively, [C_2moxa][BF_4] exhibits higher conductivity than [C_2mpyr][BF_4] (~10^{-7} S cm^{-1} at 30°C) (Iranipour et al., 2017), *N*,*N*-diethylpyrrolidinium [C_2epyr][BF_4] (2×10^{-9} S cm^{-1} at 30°C) (Yunis et al., 2018a), [HMG][BF_4] (not measurable at ambient temperature) (Yunis et al., 2019) and [C_1moxa][BF_4] (~5×10^{-7} S cm^{-1} at 30°C) (Kang et al., 2021) plastic crystals. Consequently, [C_2moxa][BF_4] holds significant potential as an electrolyte and is worth further exploration by mixing with $LiBF_4$ salts. The [C_2moxa][PF_6] exhibited a good conductivity of 6×10^{-6} S cm^{-1} at 30°C, which is higher than its methyl-substituted equivalent, [C_1moxa][PF_6], which has a conductivity on the order of 10^{-9} S cm^{-1} at 30°C (Kang et al., 2021). Previously reported OIPCs, such as [C_2epyr][PF_6] (3.6×10^{-6} S cm^{-1} at 30°C) (Yunis et al., 2018a), [HMG][PF_6] (not measurable at ambient temperature) (Yunis et al., 2019), [$C_{(i3)}$mpyr][PF_6] (~4×10^{-10} S cm^{-1} at 30°C) (Al-Masri et al., 2020a) and *N*-methoxymethyl trimethylammonium [$N_{111,101}$][PF_6] (1.4×10^{-8} S cm^{-1} at 30°C) (Warrington et al., 2022) exhibited lower conductivities with the $[PF_6]^-$ anion. The higher conductivity of [C_2moxa][PF_6] can primarily be attributed to the solid-solid phase transition at 18°C that has a relatively large $\Delta S_{II\text{-}I}$ of 42 J mol^{-1} K^{-1}, which results in a more disordered phase I (Table 1). The calculated activation energies (E_a) for the OIPCs, [C_2moxa][BF_4], [C_2moxa][PF_6] and [C_2moxa][FSI] and ionic liquid [C_2moxa][FTFSI] are included in Supplementary Table S10.

The [C_2moxa][TFSI] salt showed a conductivity of approximately 2×10^{-7} S cm^{-1} at 30°C, which is two orders of magnitude higher than its non-ether counterpart [C_2mpyr][TFSI] (4×10^{-9} S cm^{-1} at 30°C, T_m= 86°C) (MacFarlane et al., 1999; Nti et al., 2021). Notably the methyl-substituted [C_1moxa][TFSI] salt also exhibited a similar conductivity of 10^{-7} S cm^{-1} at 30°C (Kang et al., 2021). The higher conductivity of [C_2moxa][TFSI] at ambient temperature can be attributed to the higher $\Delta S_{II\text{-}I}$ of 18 J mol^{-1} K^{-1} compared to the [C_2mpyr][TFSI] ($\Delta S_{II\text{-}I}$ = 3 J mol^{-1} K^{-1}) indicating more disorder. As for other OIPCs, the conductivity of [C_2moxa][TFSI] experiences a sharp increase after melting at 51°C, reaching 10^{-3} S cm^{-1}. This significant enhancement in ionic conductivity for [C_2moxa][TFSI] aligns with the material's transition from a solid to a liquid state, where ions become highly mobile near the melting point and after. This is further supported by static NMR spectra (^{1}H) showing a superimposed narrow peak (~2 kHz) from 30°C onward, indicating the presence of an increasing proportion of mobile cations.

The oxazolidinium OIPC salts demonstrate superior ionic conductivities compared to their pyrrolidinium counterparts. Notably in the case of $[BF_4]^-$ and $[TFSI]^-$ -based OIPCs, [C_2moxa][BF_4] displays conductivity about an order of magnitude higher than [C_2mpyr][BF_4] (Iranipour et al., 2017) (8×10^{-6} vs. 7×10^{-7} S cm^{-1} at 30°C respectively). Moreover [C_2moxa][TFSI] also outperforms [C_2mpyr][TFSI] (2×10^{-7} vs. 4×10^{-9} S cm^{-1} at 30°C) (MacFarlane et al., 1999; Nti et al., 2021). Kang et al. reported the [C_2moxa][FSI] is around three times more conductive than [C_2mpyr][FSI] (6×10^{-6} vs. 2×10^{-6} S cm^{-1} at 30°C) (Kang et al., 2021). Additionally, when comparing the ethyl-substituted salts $[C_2\text{moxa}]^+$ to methyl-substituted counterparts $[C_1\text{moxa}]^+$, the latter shows lower conductivities, highlighting the benefit of the ethyl chain (Kang et al., 2021). However, it is worth mentioning that previously reported oxazolidinium ILs like [C_4moxa][TFSI] showed a lower conductivity value than [C_4mpyr][TFSI] (2×10^{-3} vs. 3×10^{-3} S cm^{-1} at 25°C) indicating a contrast in the ionic conductivity trend depending on whether the salt is an ionic liquid or an OIPC (Zhou et al., 2006). This probably indicates an influence of variations in the interactions and transport mechanisms of solids and liquids. Nonetheless, it is clear that incorporating a five-membered cyclic ether cation into an OIPC structure is advantageous for ionic conductivity.

4.3 Solid-state NMR analysis

Solid-state nuclear magnetic resonance (NMR) spectroscopy is highly valuable for investigating molecular motion and ion dynamics within OIPCs (García and O'Dell, 2022). Unlike the sharp peaks seen in the NMR spectra of liquid solutions, static NMR spectra of solid powder samples exhibit broader peaks. The presence of disorder in OIPCs can lead to both narrow and broad peaks, indicating the presence of mobile or less mobile components respectively within the material. The full width at half-maximum (FWHM) values obtained from such spectra, as well as the chemical shift anisotropy (CSA) that arises due to the orientation-dependent electron shielding environment of the nuclei, provide insights into the relative mobility of the ions. Additionally, the relative intensity values quantitatively indicate the percentage of mobile or less mobile cations/anions, further enhancing the depth of information that can be achieved through NMR analysis (Zhu et al., 2014; Zhu and O'Dell, 2021).

In this study, solid-state NMR spectroscopy was used to investigate the ion dynamics of the OIPCs: [C_2moxa][TFSI], [C_2moxa][BF_4], and [C_2moxa][PF_6] across a range of temperatures from −20°C–50°C. By comparing the ^{1}H NMR spectra of all three salts, the dynamics of the cation was studied. Additionally, the presence of ^{19}F in the $[TFSI]^-$, $[BF_4]^-$, and $[PF_6]^-$ allowed investigation of the dynamics of the anion. To gain further insights, ^{11}B NMR spectra were also analysed for the [C_2moxa][BF_4] salt. The use of multiple NMR nuclei enables a better understanding of both cation and anion dynamics.

The static ^{1}H spectrum of [C_2moxa][BF_4] (Figure 5A, orange spectra) follows an unusual trend with heating. At 0°C, the linewidths of the broad and narrow peaks are measured as 9.8 and 1.4 kHz, respectively (Figure 6A). Upon increasing the temperature from 0°C to 20°C, the linewidth of the narrow peak surprisingly increases. One possible interpretation of this behavior is that, in phase II, there are two distinct populations of cations, each exhibiting different levels of mobility. After the solid-solid phase transition at 10°C, phase I shows only one population of cations with intermediate mobility. At temperatures above 20°C, a small sharper component becomes visible, suggesting that the dynamics of a small proportion of the cations have substantially increased. It is important to highlight that

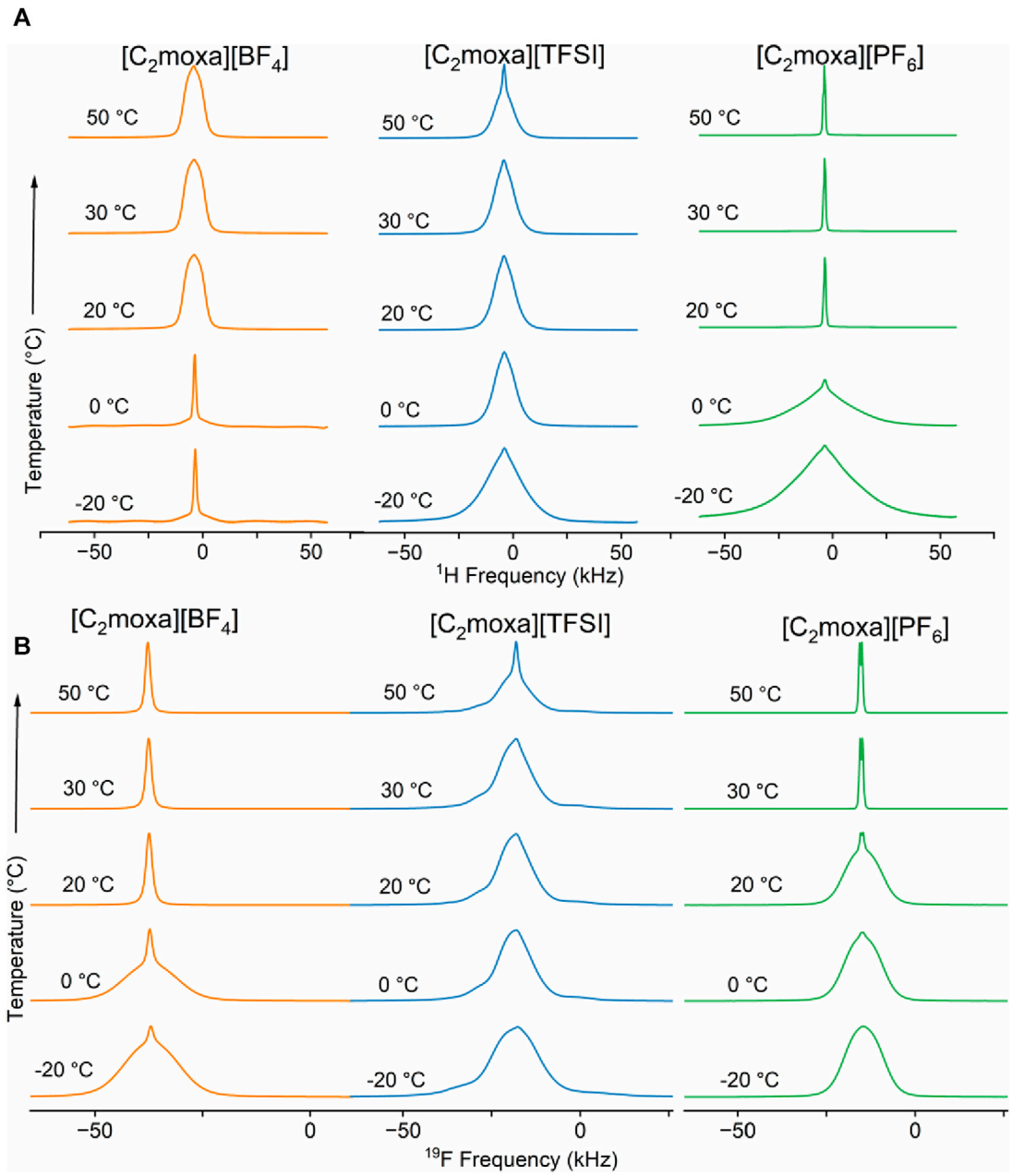

FIGURE 5
(A) ^{1}H **(B)** ^{19}F static NMR of $[C_2moxa]^+$ salts at five different temperatures: −20, 0, 20, 30°C and 50°C.

the unusual increase in linewidth observed from 0°C to 20°C, is specific and reproducible for ^{1}H spectra of the cation and is not mirrored in the ^{19}F spectra of the anion.

The relative intensity of the broad and narrow component as a function of temperature correlates with the fraction of mobile/less mobile species (Figures 6C,D). Even in phase II, a significant number of mobile cations (approximately 56% at 0°C) compared to less mobile cations (approximately 44% at 0°C) highlights the disorder of the $[C_2moxa][BF_4]$ OIPC. The ^{19}F NMR spectra shows a sudden decrease in linewidth observed at 20°C. As the temperature is further increased, the linewidth of the narrow component gradually decreases, indicating an increase in anion dynamics. The static ^{11}B NMR spectra (Figure 6E) also confirm the increased dynamics of the anions, as a significant decrease in linewidth is observed from 0°C to 20°C.

The ^{1}H NMR spectra of both $[C_2moxa][TFSI]$ and $[C_2moxa][PF_6]$ display a broad peak alongside a narrow peak, indicating the presence of relatively mobile and immobile cation species at −20°C and 0°C temperatures. (Figure 5A blue and green spectra, respectively). As the temperature increases, the intensity of the narrow peak rises for both salts, signifying a relative increase in the population of dynamic cations. At 0°C, the ^{1}H FWHM linewidths of the $[C_2moxa][PF_6]$ salt for the broad and narrow peaks are 28.5 and 2.4 kHz, respectively. However, at 20°C, the broad peak intensity decreases, leaving only the narrow component with a linewidth of 1.2 kHz. The sudden increase in disorder can be

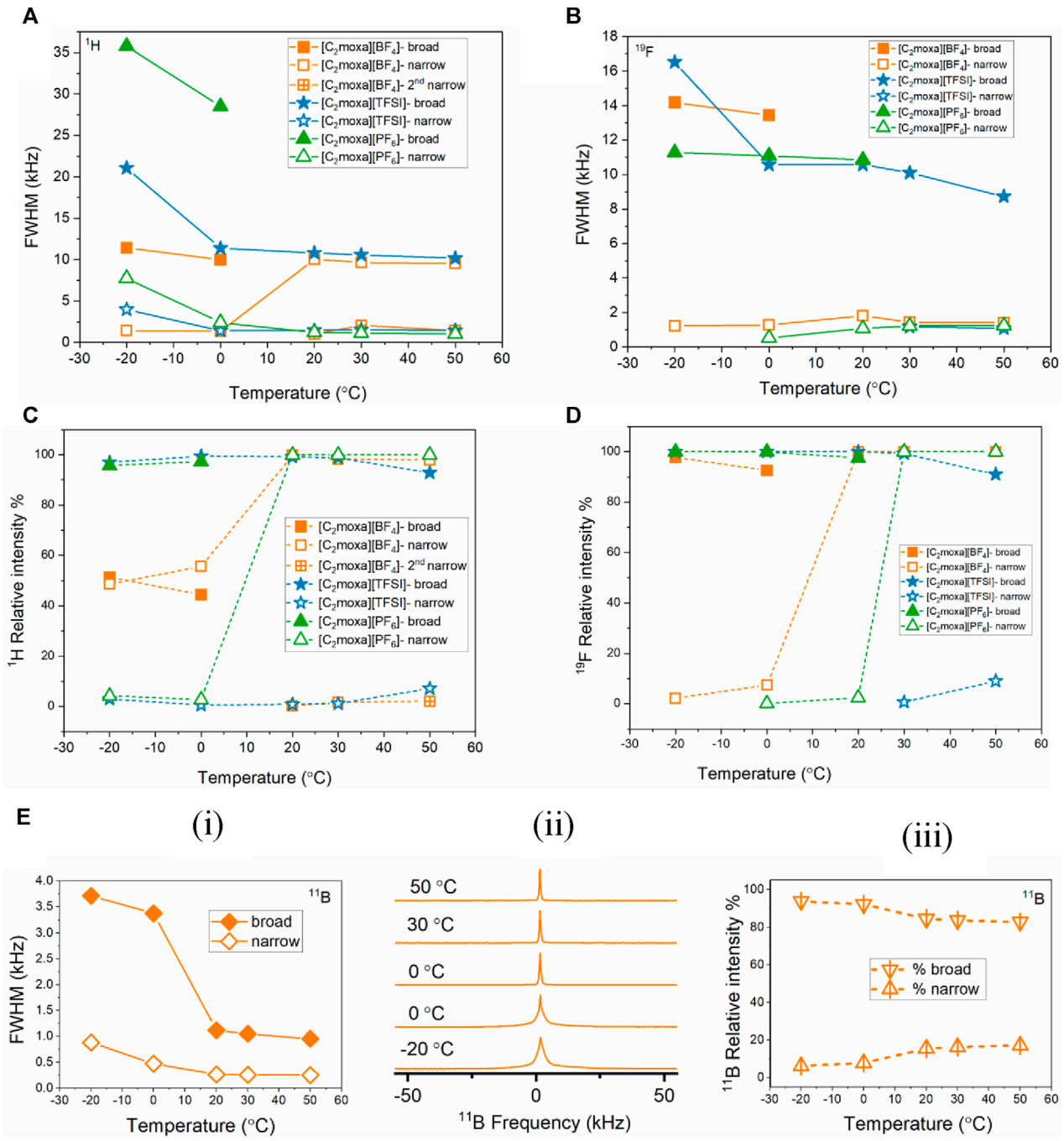

FIGURE 6
(A) and **(B)** ^{1}H and ^{19}F FWHM values for [C$_2$moxa]$^{+}$ salts respectively. **(C)** and **(D)** ^{1}H and F % relative intensity values for [C$_2$moxa]$^{+}$ salts respectively. **(E)** **(i)**, **(ii)**, and **(iii)** FWHM, signal pattern and % relative intensity values of ^{11}B nucleus respectively.

correlated with the high $\Delta S_{II\text{-}I}$ of 42 J mol^{-1} K^{-1}. Moreover Figure 5 (green) indicates that ^{1}H spectra of [C$_2$moxa][PF$_6$] starts to narrow at 20°C (aligning with the phase II-I transition), while the ^{19}F spectra narrow only after reaching 30°C. This suggests that the cationic component of [C$_2$moxa][PF$_6$] initiates ion dynamics before the anions. In contrast, at 20°C, [C$_2$moxa][TFSI] exhibits both broad and narrow peaks (~10.8 and ~1.5 kHz, respectively), indicating the persistence of relatively immobile/static species even in phase I. From 20°C to 50°C, [C$_2$moxa][PF$_6$] displays consistently narrower linewidths, while [C$_2$moxa][TFSI] continues to exhibit both broad and narrow components. In the ^{19}F NMR spectra of [C$_2$moxa][TFSI], chemical shift anisotropy (CSA) patterns are observed across the studied temperature range, suggesting slow dynamics of the anions. However, at 30°C and 50°C, a small narrow peak also appears alongside the asymmetric CSA peak of the [C$_2$moxa][TFSI] spectra representing the presence of a small fraction of more mobile anions.

Figure 6D illustrates that only 9% of the [TFSI]$^{-}$ anions exhibit relatively high mobility, even near the melting

TABLE 2 Onset potentials of cathodic (E_{CL}) and anodic (E_{AL}) decomposition and the electrochemical stability windows, ΔE, of the salts dissolved in acetonitrile, with tetrabutylammonium hexafluorophosphate ($TBAPF_6$, 0.1 M) as the supporting electrolyte, as determined by the cyclic voltammetry at 25°C (Figure 7).

Material	E_{CL} (V vs Fc/Fc$^+$)	E_{AL} (V vs. Fc/Fc$^+$)	EW (V)
[C_2moxa][BF_4]	−3.2	+1.6	4.8
[C_2moxa][TFSI]	−2.0	+2.1	4.1
[C_2moxa][PF_6]	−1.6	+2.1	3.7
[C_2moxa][FTFSI]	−1.7	+2.0	3.7

temperature (T_m = 51°C), suggesting that the majority of [TFSI]$^-$ anions do not significantly contribute to the ion dynamics of this salt. In contrast, at 30°C and 50°C, all of the [C_2moxa][PF_6] anions (~100% ^{19}F relative intensity) demonstrate higher rotational mobility, contributing to the high degree of disorder in the salt.

4.4 Electrochemical stability

The electrochemical stability window (EW) defines the potential range within which the OIPC remains stable without undergoing oxidation or reduction. Wide EW values allow for the use of higher voltage cathodes, which can lead to higher power density in batteries (Huo et al., 2023). Here we removed the known adverse effects of halide ions on electrochemical stability (Passerini and Appetecchi, 2013) by synthesising the new OIPCs via the tosylate intermediate rather than the halide route (Kang et al., 2022). To assess the suitability of these salts as electrolytes, their EW values were measured using cyclic voltammetry (CV) (Table 2, Figure 7. The EW was identified based on the reduction (cathodic limiting) potential and the oxidation (anodic limiting) potential which are denoted as E_{CL} and E_{AL}, respectively. Both E_{CL} and E_{AL} values were determined based on a cut-off current density of 0.2 mA cm^{-2}. All experiments were conducted using the OIPCs dissolved in acetonitrile (1 g L^{-1}); the high melting point of some of these OIPCs prohibited measurement in the molten state and led to poor contact in the solid state so all were tested in acetonitrile to allow accurate comparison.

For comparison, the EW of [C_2moxa][FSI] was determined using the same Pt three electrode system, yielding a value of 3.8 V. This measurement is in good agreement with the value of 3.9 V reported by Kang et al. (Kang et al., 2021) The slight variation from the reported electrochemical window of [C_2moxa][FSI] may be attributed to variations in the experimental conditions: here, the EW was analysed for the neat material dissolved in acetonitrile (1 g L^{-1}) at room temperature, while the literature value for the neat material was measured at 70°C.

The [C_2moxa][TFSI] salt exhibited a wider EW (4.1 V) compared to [C_2moxa][FSI] (3.8 V). This finding supports the conclusions presented in prior literature that [TFSI]$^-$ based salts possess greater electrochemical stability than [FSI]$^-$ based salts, for example, [C_3mpyr][TFSI] (6.1 V)> [C_3mpyr][FSI] (5.1 V); *N*-propyl-*N*-methyl piperidinium [C_3mpip][TFSI] (6.8 V)> [C_3mpip][FSI] (5.8 V); *N*-ethoxymethyl-*N*-methyl pyrrolidinium [C_{201}mpyr][TFSI] (5.6 V)>[C_{201}mpyr][FSI] (5.4 V). (Reiter et al., 2013; Jeong et al., 2019).

The EW of 4.8 V for [C_2moxa][BF_4] was determined to be the widest among the studied salts, with a E_{CL} of −3.2 V and a E_{AL} of +1.6 V. This EW is approximately 0.4 V higher than the reported EW of the well-known [C_2mpyr][BF_4] salt at 100°C (Shekibi et al., 2012), although it should be noted that different experimental conditions were used. On the other hand, [C_2moxa][PF_6] showed an EW of 3.7 V, with a E_{CL} of −1.6 V and an E_{AL} of +2.1 V. It is important to note that while the reduction potential is primarily influenced by the cationic structure, the anionic structures can also affect the reduction behaviour and *vice versa* (Yeon et al., 2005; Zhou et al., 2006).

When comparing oxazolidinium salts with their pyrrolidinium analogues, in most cases the latter exhibit a wider EW. For example, the EW of [C_2moxa][TFSI] (4.1 V) is smaller than that of [C_3mpyr][TFSI] (6.1 V) (Lethesh et al., 2022). Similarly, [C_2moxa][FSI] has an EW 0.5 V smaller than [C_2mpyr][FSI] (Kang et al., 2021) and [C_2moxa][FTFSI] (3.7 V) has a narrower EW compared to [C_3mpyr][FTFSI] (5.5 V) (Reiter et al., 2013). Notably, [C_2moxa][BF_4] exhibits an EW of 4.8 V, while [C_2mpyr][BF_4] has an EW of 4.4 V (Shekibi et al., 2012). However, it is worth noting that these differences could be influenced by variations in experimental conditions and the type of electrodes used.

Prior literature also shows that the presence of an ether bond in the side chain or cationic core of the cation generally reduces electrochemical stability. The *N*-butyl-*N*-methylmorpholinium [C_4mmor][TFSI] was reported to have an EW of 4.5 V, whereas the piperidinium analogue with a slightly shorter alkyl chain, [C_3mpip][TFSI], had an EW of 5.8 V (Matsumoto et al., 2006; Lane, 2012). Replacement of propyl group in [C_3mpyr][TFSI] with methoxy ethyl group in [C_{102}mpyr][TFSI] reduced the EW from 6.4 to 5.9 V (Lethesh et al., 2022). The underlying reasons for this instability could be the facile reduction of the ether moiety, potentially leading to alkoxide formation, or enhanced reduction of the quaternary ammonium center (Lane, 2012), although, the exact mechanism is still not clear. Nevertheless, the initial assessment of the new ethyl oxazolidinium-based salts demonstrates promising electrochemical stability, justifying further exploration of their potential application in Li electrochemistry.

5 Development of oxazolidinium-based electrolytes

Two oxazolidinium OIPCs, [C_2moxa][BF_4] and [C_2moxa][FSI], were chosen for investigation of their use as lithium electrolytes. The [C_2moxa][BF_4] salt because it showed a high conductivity of 8 × 10^{-6} S cm^{-1} at 30°C, which is approximately an order of magnitude

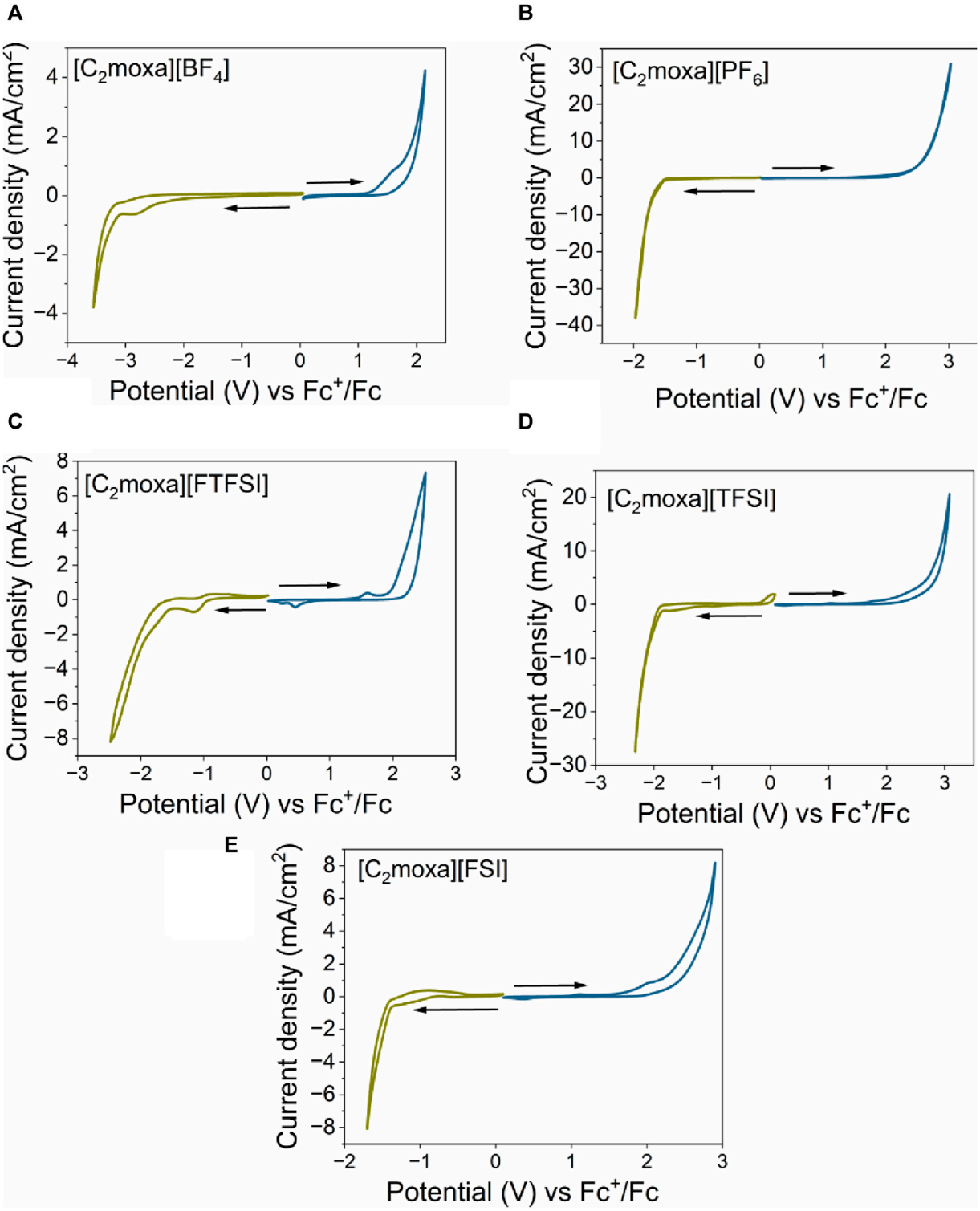

FIGURE 7
Cyclic voltammetry of **(A)** [C_2moxa][BF_4], **(B)** [C_2moxa][PF_6], **(C)** [C_2moxa][FTFSI] **(D)** [C_2moxa][TFSI] and **(E)** [C_2moxa][FSI]. All experiments were conducted at 25°C at a scan rate of 50 mV s^{-1}, with a Pt working electrode (WE), Pt coil coulombic efficiency, and Pt wire reference electrode. Ferrocene was used as an internal reference (Fc/Fc^+ peak E_m [C_2moxa][BF_4]= −0.05 V; E_m [C_2moxa][PF_6]= −0.03 V; E_m [C_2moxa][FTFSI]= −0.02 V; [C_2moxa][TFSI] = −0.08 vs Pt). blue colour scan indicates the anodic trace. green colour scan indicates the cathodic trace.

greater than its pyrrolidinium counterpart. The [C_2moxa][FSI], because it displayed multiple solid-solid phase transitions at low temperatures (−96, −74, −58, −44°C) and has a conductivity of 6 × 10^{-6} S cm^{-1} at 30°C (3 times higher than [C_2mpyr][FSI]) (Kang et al., 2021). Also, both of these salts have a wide phase I range (>100°C) and low ΔS_f values (Table 1). Consequently, these salts emerged as

strong candidates for electrolyte development. Despite exhibiting the highest conductivity in its neat state, [C_2moxa][FTFSI] was not selected for further electrolyte development as it is a room temperature ionic liquid, and our main focus was on exploring OIPCs for advanced electrolyte development.

The choice to investigate compositions with 10, 20, and 50 mol% lithium salts in these OIPCs was informed by prior research. A composite of 10 mol% $LiBF_4$ in [C_2mpyr][BF_4] showed excellent properties, with consistent conductivity around 10^{-3} S cm^{-1} over a wide temperature range in phase I (Shekibi et al., 2012). This system also demonstrated highly reversible Li plating and stripping. Adding 10 mol% LiFSI to [C_2mpyr][FSI] significantly increased conductivity compared to its 1 mol% LiFSI system (Abu-Lebdeh et al., 2006; Zhou et al., 2017a). Similarly, adding 10 mol% LiTFSI to a pyrazolium imide salt increased conductivity fivefold across the temperature range, reaching 6.9 × 10^{-4} S cm^{-1} at 5°C within its plastic crystal phase (Abu-Lebdeh et al., 2006). Additionally, studies on high Li salt concentrations supported this approach. For instance, [C_2mpyr][FSI] with 50 mol% LiFSI exhibited conductivity four orders of magnitude higher (~10^{-4} S cm^{-1}) than neat [C_2mpyr][FSI] ((~10^{-8} S cm^{-1}) at 20°C (Zhou et al., 2017b). In the tetramethyl isobutylphosphonium [P_{111i4}][FSI]/50 mol% FSI system, efficient Li plating and stripping indicated high electrolyte stability (Girard et al., 2015). Moreover, [C_2epyr][FSI]/50 mol% LiFSI supported a cycling efficiency of 96% over 100 cycles in a lithium symmetrical cell (Al-Masri et al., 2018). Here, the 20 mol% composition was also chosen to strike a balance between maintaining a quasi-solid phase for enhanced stability and providing sufficient Li^+ concentration for effective Li electrochemistry. This choice was further supported by favorable results from previous studies involving 20 mol% electrolyte mixtures in sodium and lithium systems (Iranipour et al., 2017; Makhlooghiazad et al., 2017).

5.1 Thermal behaviour

As previously discussed, the neat [C_2moxa][BF_4] exhibited a solid-solid phase transition at 10°C and melted at 130°C. When 10 mol% Li salt was added, the melting peak broadened and decreased to 98°C, indicating a phase transition at around 11°C (Figure 2B). With 20 mol% Li salt, the melting peak merged with the 11°C peak, resulting in dual peaks at 13°C and 23°C, along with a cold crystallization peak at −63°C indicating supercooling which is commonly seen in ILs with ether functionalities (Galiński et al., 2006). In contrast, the 50 mol% system displayed quasi-solid behavior with a broad melting point at 87°C, without additional peaks below the melting transition. Based on the observed thermal behaviour of the [C_2moxa][BF_4] electrolytes, it is tentatively concluded that the eutectic composition is around 25 mol% Li salt, although complete phase diagram mapping would be necessary to confirm this, which is beyond the current scope of this work.

Neat [C_2moxa][FSI] shows two distinct solid-solid phase transitions at −95°C and −44°C, along with smaller peaks at −74 and −58°C, consistent with our prior report (Kang et al., 2021). This material maintains a broader phase I range from −44°C to its melting point at 127°C. In the case of the 10 mol% LiFSI system, the solid-solid transitions closely resemble those of the neat OIPC. However, the melting point is lowered and broadened to 97°C, with the material displaying quasi-solid state characteristics. Upon increasing the Li ion concentration to 20 mol%, the thermal behavior undergoes a significant shift. The low-temperature transition peaks disappear, being replaced by a glass transition (T_g) at −84°C for the ionic liquid. The 50 mol% FSI phase behavior also differs markedly from the neat and 10 mol% system, revealing only a T_g at −67°C in the latter (Figure 2B). This shift in T_g to higher temperatures upon increasing the Li ion concentration aligns with findings in prior literature (Girard et al., 2015; Yoon et al., 2015). Other reports of 50 mol% LiFSI mixed into OIPCs have also reported the production of a liquid phase at RT, including tetramethyl cyanoammonium FSI [N_{111CN}][FSI] (T_g = −54°C) (Yunis et al., 2020b), [C_3mpyr][FSI] (T_g = −73°C) (Yoon et al., 2015), [C_2mpyr][FSI] (T_g= −81°C) (Zhou et al., 2017b), [C_2epyr][FSI] (T_g = −75°C) (Al-Masri et al., 2018), and [P_{111i4}][FSI] (T_g = −73°C). (Girard et al., 2015).

5.2 Ionic conductivity

Figure 4B illustrates the temperature-dependent ionic conductivity of [C_2moxa][BF_4], [C_2moxa][FSI], and their mixtures with Li salts. Upon adding 10 mol% $LiBF_4$ to [C_2moxa][BF_4], the conductivity experiences a two-fold increase, reaching 2 × 10^{-4} S cm^{-1} at 30°C. The addition of 20 mol% $LiBF_4$ results in an even higher conductivity, nearly doubling the previous value to 4 × 10^{-4} S cm^{-1} at 30°C. When 50 mol% $LiBF_4$ is added, the ionic conductivity decreases to 3 × 10^{-5} S cm^{-1} at 30°C, although it still represents an improvement in conductivity compared to the neat [C_2moxa][BF_4] salt.

This behavior of the BF_4 electrolyte mixtures can be attributed to the physical state of the mixtures at ambient temperature: the 20 mol% system, as an ionic liquid, exhibits higher conductivity compared to the 10 mol% and the 50 mol% systems, both of which exhibit quasi-solid-state behavior. The ionic conductivity of the 10 mol% system surpasses that of the 50 mol% system, suggesting a greater presence of the liquid phase in the former. The quasi -solid state can be explained by the presence of the mixed salt liquid phase which is dispersed in [C_2moxa][BF_4] solid phase, possibly within the grain boundaries (Montanino et al., 2012). When the temperature is increased, in addition to the increase in ion mobility, the fraction of the liquid phase also increases, and when the 50 mol% $LiBF_4$ system completely melts the conductivity reaches 2 × 10^{-3} S cm^{-1} at 90°C. On the other hand, the conductivity of the 10 mol% $LiBF_4$ system is very similar to the 20 mol% $LiBF_4$ system between 80°C and 100°C. Thus, there appears to be a balance between the advantage of increasing the concentration of small charge carriers (20 mol% > 10 mol%) and the parallel increase in viscosity associated with high salt concentrations.

It is worth noting that 10 and 20 mol% mixtures of $LiBF_4$ in [C_2mpyr][BF_4] (i.e., with the pyrrolidinium cation) showed a different trend, where elevating the lithium salt concentration from 10 to 20 mol% initially led to a slight decline in conductivity at 30°C, followed by an increase in conductivity at higher temperatures. Nonetheless, both 10 and 20 mol% [C_2mpyr][BF_4] electrolytes displayed lower conductivities at 30°C (~10^{-4} S cm^{-1} and

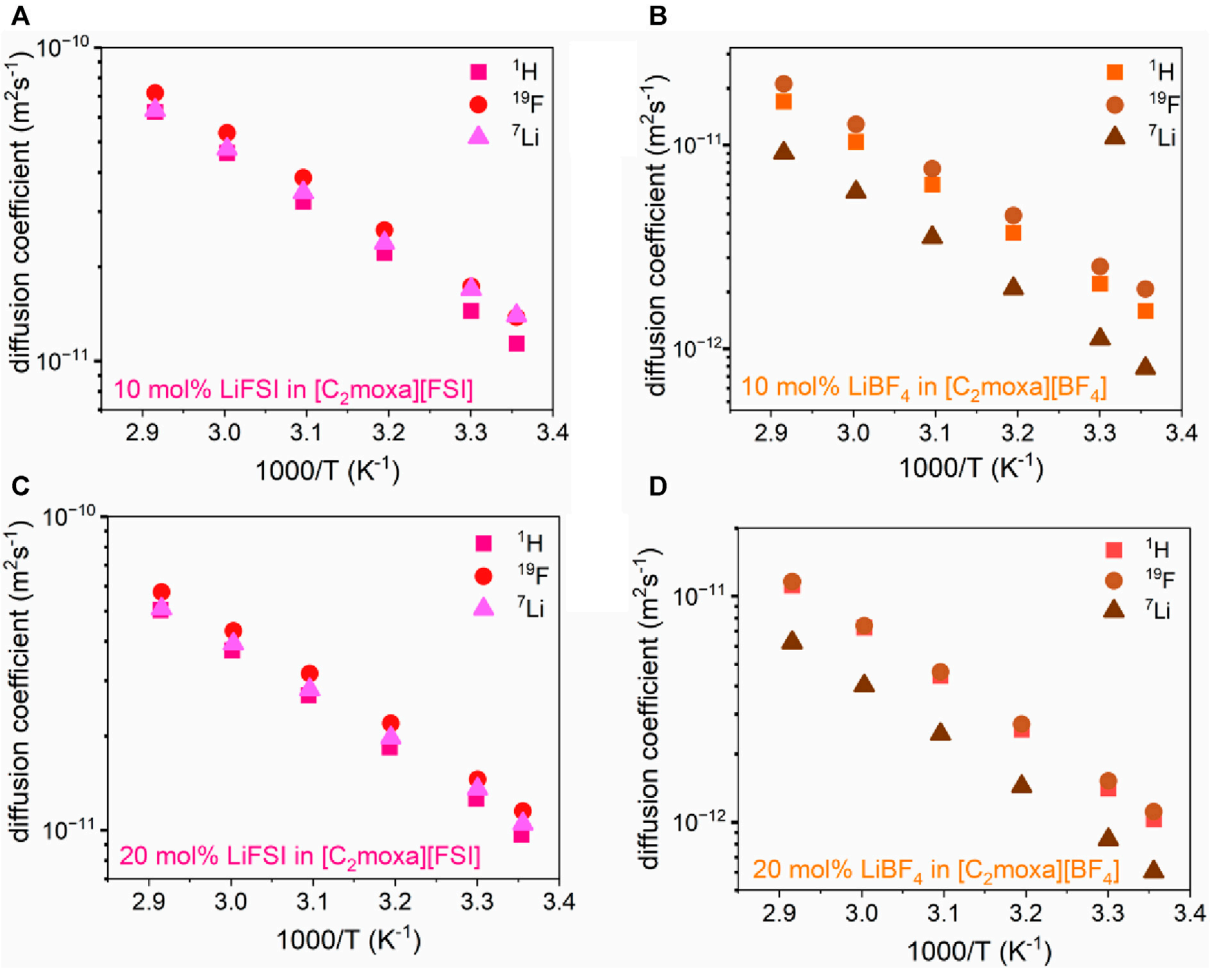

FIGURE 8
Temperature dependent self-diffusion coefficients (^{1}H: cation, ^{19}F: anion, ^{7}Li: lithium cation) of **(A)** 10 mol% LiFSI in [C_2moxa][FSI] **(B)** 10 mol% $LiBF_4$ in [C_2moxa][BF_4] **(C)** 20 mol% LiFSI in [C_2moxa][FSI] **(D)** 20 mol% $LiBF_4$ in [C_2moxa][BF_4], in temperature range 25°C–70°C.

~10^{-5} S cm^{-1}, respectively) compared to the equivalent electrolytes made with the oxazolidinium salts (Iranipour et al., 2017).

The addition of 10 mol% LiFSI to [C_2moxa][FSI] results in a substantial increase in conductivity compared to the neat OIPC, with the value rising from 4×10^{-6} S cm^{-1} to 8×10^{-4} S cm^{-1} at 30°C. Notably the conductivity for the 10 mol% LiFSI system (a quasi-solid electrolyte) is very similar to the 50 mol% LiFSI system (a liquid electrolyte) at low temperature (8×10^{-4} S cm^{-1} at 30°C). However, when the 10 mol% LiFSI system melts, it exhibits higher conductivity than the 50 mol% LiFSI system likely due to a lower viscosity with lower salt content. Also, the 10 and 20 mol% LiFSI systems show similar conductivity from 80°C to 100°C, reaching the magnitude of 10^{-2} S cm^{-1}. As indicated above, the 50 mol% LiFSI has a higher glass transition temperature (T_g = −67°C) than 20 mol% LiFSI (T_g = −84°C), which is consistent with the lower conductivity of the 50 mol% LiFSI mixture. This aligns with the well-known trend in ionic liquid data, where an increase in the lithium salt concentration leads to an elevated T_g and subsequently reduced conductivity, primarily due to the increased viscosity (Martinelli et al., 2009; Wu et al., 2014). The conductivity of the 50 mol% LiFSI in [C_2moxa][FSI] is a little lower than 50 mol% LiFSI in [C_2epyr][FSI] (3×10^{-3} S cm^{-1} at 30°C) (Al-Masri et al., 2018), 50 mol% LiFSI in [C_3mpyr][FSI] (1.5×10^{-3} S cm^{-1} at 30°C) (Yoon et al., 2015), 50 mol% LiFSI in [P_{111i4}][FSI] (1×10^{-3} S cm^{-1} at 30°C) (Girard et al., 2015), but higher than 50 mol% LiFSI in [C_2mpyr][FSI] (6×10^{-4} S cm^{-1} at 30°C) (Zhou et al., 2017b), 50 mol% LiFSI in [$C_{(i3)}$mpyr][FSI] (7×10^{-4} S cm^{-1} at 30°C) (Al-Masri et al., 2020b) and 50 mol% LiFSI in [N_{111CN}][FSI] (6×10^{-4} S cm^{-1} at 30°C) (Yunis et al., 2020b). The correlation between T_g and conductivity holds across these salt systems, where a higher T_g tends to result in lower conductivity.

In summary, this study reveals that 10, 20, and 50 mol% $LiBF_4$ mixtures with [C_2moxa][BF_4] have lower conductivity compared to the LiFSI counterparts in [C_2moxa][FSI] electrolytes, despite neat [C_2moxa][BF_4] having a slightly higher conductivity (6×10^{-6} S cm^{-1} vs. 8×10^{-6} S cm^{-1} respectively). The crucial factor influencing the enhanced ionic conductivity of FSI-based salts is the physical state of the electrolytes. When LiFSI is combined with [C_2moxa][FSI] (20 and 50 mol%), the electrolytes become liquid leading to high conductivity. In contrast, when $LiBF_4$ is mixed with [C_2moxa][BF_4], electrolytes remained as quasi-solids across the temperature range studied resulting in lower conductivity. The trend aligns with previous findings, where neat [N_{111CN}][BF_4] showed higher conductivity than neat

$[N_{111CN}][FSI]$, but when 10 and 50 mol% Li mixtures were introduced, the FSI electrolytes exhibited higher conductivities (Yunis et al., 2020b). The lower ionic conductivity of $LiBF_4$ mixtures than LiFSI mixtures may be due to Li^+ being less dissociated from $[BF_4]^-$ than $[FSI]^-$. This is supported by slower self-diffusion of $[BF_4]^-$ compared to $[FSI]^-$ in 10 and 20 mol% electrolytes for both systems, as determined through NMR analysis discussed next. Computational simulations of Li salt/IL systems have indicated stronger binding between Li^+ and BF_4^- (592.2 kJ mol^{-1}) compared to Li^+ and FSI^- (505.7 kJ mol^{-1}) (Chen and Forsyth, 2019). This can be attributed to FSI^- being a larger, more diffuse anion, resulting in weaker interaction with Li^+ cations. Also, visually the viscosity of the liquid compositions with $LiBF_4$ system is higher than the LiFSI, which would result in a lower conductivity.

5.3 Self-diffusion coefficients

Pulsed field gradient stimulated echo (PFG-STE) NMR spectroscopy was employed to gain direct measurement of the translational motion of ions within the 10 and 20 mol% electrolytes systems of both $[C_2moxa][BF_4]$ and $[C_2moxa][FSI]$. The 50 mol% mixtures in both systems were excluded due to their comparatively lower conductivity (Figure 4B, Supplementary Table S2). This NMR technique allowed a comparison of the mobility of lithium (^7Li) within the electrolyte with that of the cation $[C_2moxa]^+$ and anions ($[FSI]^-$ and $[BF_4]^-$), represented by ^1H and ^{19}F, respectively (García and O'Dell, 2022).

PFG NMR data shows that anions diffuse faster than the cations and Li^+ across all four systems. This trend has been observed in other similar OIPC/IL systems (Bayley et al., 2011; Girard et al., 2015). Also, the diffusivity values for all ions (D_{H^+}, D_{F^-}, and D_{Li^+}) in the $[C_2moxa][FSI]$ electrolyte mixtures (ranging from 10^{-11} to 10^{-12} m^2 s^{-1}) were higher than the $[C_2moxa][BF_4]$ electrolytes (ranging from 10^{-12} to 10^{-13} m^2 s^{-1}) at all temperatures. This is consistent with the higher ionic conductivity observed in the former.

In the $[C_2moxa][FSI]$ electrolyte systems, the diffusivity values of $[C_2moxa]^+$, $[FSI]^-$, and Li^+ were found to be very similar at the various temperatures examined. However, in the $[C_2moxa][BF_4]$ systems, a clear difference in the diffusivity of the Li^+, compared to both the $[C_2moxa]^+$ cation and $[BF_4]^-$ anion becomes evident, with lithium diffusing at a notably slower rate than both the cation and the anion respectively (Figure 8B,D). The diffusivity ratio values for Li^+ (the ratio between the Li^+ diffusion coefficient and the sum of the diffusion coefficients of all ions) are shown in Supplementary Table S4.

However, an intriguing observation was made when increasing the salt concentration from 10 to 20 mol% Li salt; the diffusion coefficients for all ionic species became slower in both $[C_2moxa][FSI]$ and $[C_2moxa][BF_4]$ electrolyte mixtures. This behavior aligns with a prior report that showed that increased LiFSI concentration in $[C_3mpyr][FSI]$ resulted in decreased ion diffusivity at 25°C (Yoon et al., 2015). This finding, however, contradicts the conductivity data for the electrolytes. In both $[FSI]^-$ and $[BF_4]^-$ mixtures, the 20 mol% system exhibited higher conductivity than the 10 mol% system. This inconsistency can be explained by considering that PFG NMR measures diffusion from all species, including neutral ion pairs/aggregates, whereas ionic conductivity measurements solely assess charge carriers. Therefore, ion clusters or aggregates are expected to be less mobile due to their larger ion size, lowering the average self-diffusion coefficient measured by PFG NMR but not affecting the conductivity values (Popov et al., 2020). Hence, the difference in behavior between the 10 and 20 mol% systems may be attributed to their respective physical states. The 10 mol% systems, behaving as quasi-solids, promote more ionic interactions, leading to higher diffusivity but lower conductivity. On the other hand, the 20 mol% systems, functioning as liquid electrolytes, exhibit fewer ionic interactions, resulting in higher conductivity but reduced diffusivity.

5.4 Lithium electrochemistry

In lithium metal batteries, efficient lithium deposition and stripping are critical for cycling performance. It is essential that the solid electrolyte interphase (SEI) remains stable and possesses the capability to facilitate efficient lithium-ion conduction (Liu et al., 2017). Thus, we investigated the influence of oxazolidinium-based salts on lithium electrochemistry using cyclic voltammetry (CV). A preliminary quantification of cycling efficiency was obtained by estimation of the coulombic efficiency (CE), which represents the percentage of lithium stripped to lithium plated during each cycle. The electrolyte compositions of 20 and 50 mol% LiFSI in $[C_2moxa][FSI]$ were compared to 20 and 50 mol% $LiBF_4$ in $[C_2moxa][BF_4]$ electrolytes. The choice of 20 and 50 mol% systems aimed to explore the impact of high lithium concentrations on $[C_2moxa][FSI]$ and $[C_2moxa][BF_4]$ electrochemistry.

The CVs shown in Figures 9A,B clearly demonstrate distinct plating and stripping peaks, indicating that the $[C_2moxa][FSI]$ electrolyte systems can support lithium cycling. LiFSI is known to be of benefit for forming a stable, uniform, and conductive SEI layer for Li batteries (Bhatt et al., 2010). Thus, the $[FSI]^-$ anion in the studied $[C_2moxa][FSI]$ electrolyte systems could have an advantageous impact on lithium cycling. Lithium metal deposition occurred at around −3.1 V vs Fc/Fc^+ in the 20 mol% LiFSI/$[C_2moxa][FSI]$ system (Figures 9A). Multiple oxidation peaks are observed in 20 mol% LiFSI and $LiBF_4$ systems compared to 50 mol% electrolytes, during the stripping process. In the literature this phenomenon is commonly observed with a Pt WE and is attributed to the formation of Li-Pt alloy (Matsumoto et al., 2005; Wibowo et al., 2009; Yoon et al., 2013; Stachurski et al., 2023). However, it has also been suggested that during the initial stripping process, there may be variations in the coordination environment of lithium (Biernacka et al., 2020) as it is being stripped from the solid electrolyte interphase (SEI) layer, and when the SEI layer stabilizes over subsequent cycles, the stripping process becomes more uniform, resulting in a single stripping peak. Such a phenomenon may be occurring here, but detailed *in-situ* analysis would be required to confirm this. Additionally, the plating/stripping peak currents decreased gradually with cycling and suggest the progressive formation of a less conductive SEI film.

The decrease in peak currents during lithium stripping/plating is consistent with previous studies on OIPC/IL electrolyte systems: e.g., $[C_3mpip][TFSI]$/10 mol% LiTFSI (WE= Ni, 10 mV s^{-1}, 20°C) (Xu

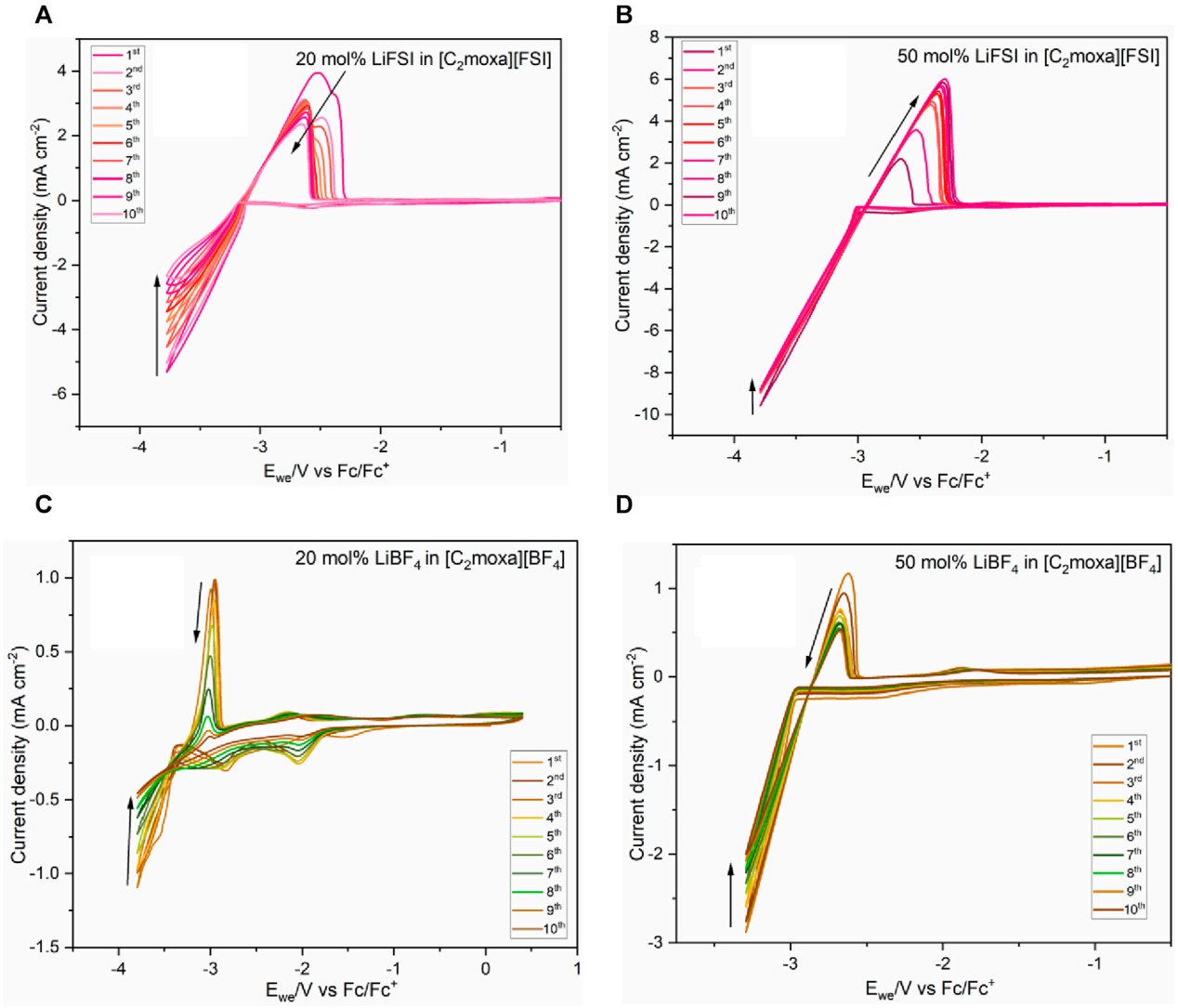

FIGURE 9
Cyclic voltammograms of the **(A)** 20 mol% LiFSI **(B)** 50 mol% LiFSI in [C_2moxa][FSI] electrolyte at RT **(C)** 20 mol% $LiBF_4$ (at RT) **(D)** 50 mol% $LiBF_4$ in [C_2moxa][BF_4] electrolyte at 50°C. Scan rate: 20 mV s^{-1}. A three-electrode cell was used in an argon glove box. WE: Ni, RE: Ag/Ag^+, counter electrode: Pt coiled wire. 10 cycles were recorded. Arrows indicate peak progression from the first to 10th scan.

et al., 2006), methyl tetrabutylphosphonium [P_{1444}][FSI]/4 mol% LiFSI (WE= Pt, 50 mV s^{-1}, 50°C) (Jin et al., 2014), [C_3mpyr][FSI]+ 0.5 mol kg^{-1} (WE= Pt, 50 mV s^{-1}, RT) (Basile et al., 2016). Moreover, the 20 mol% LiFSI/[C_2moxa][FSI] system exhibited CE ranging from 53% (first cycle) to 47% (10th cycle), indicating relatively stable lithium cycling. (Supplementary Table S5). Notably, it demonstrated the highest CE among all electrolytes analysed in this study. However, it appears to be slightly lower than reported in other FSI electrolyte systems found in the literature (Jin et al., 2014; Basile et al., 2016; Biernacka et al., 2020).

Lithium metal deposition occurred at around −2.9 V vs Fc/Fc^+ in the 50 mol% LiFSI/[C_2moxa][FSI] electrolyte (Figures 9B). Interestingly, in the 50 mol% LiFSI/[C_2moxa][FSI] electrolyte, the stripping peak current increased with cycling. This phenomenon has been noted in the literature: e.g., [HMG][FSI]/10 mol% LiTFSI (WE= Pt, 50 mV s^{-1},75°C) (Biernacka et al., 2020), in a [C_2mpyr][FSI]/50 mol% LiFSI/PVDF composite (WE= Li metal, 50 mV s^{-1}, 50°C) (Zhou et al., 2018), in [P_{111i4}][FSI]/LiFSI/PDADMA (polydialydimethylammonium)FSI (60:40:0.98 wt%) (WE= stainless steel, 20 mV s^{-1},50°C) (Yunis et al., 2018b), and for [C_3mpyr][FSI]/3.2 mol kg^{-1} LiFSI/10% DME (dimethoxyethane) (Pal et al., 2020) In previous reports an increase in the stripping peak current suggests that the active surface area of the Ni working electrode is being increased during lithium plating (Shi et al., 2001). Moreover, with each cycle, a larger charge is passed, resulting in increased lithium deposition as indicated by the larger stripping peak area. The 50 mol% LiFSI/[C_2moxa][FSI] electrolyte exhibited an initial CE of 8% (first cycle) and reached approximately 32% (ninth cycle, Supplementary Table S6).

Prior literature reports show that when Ni is used as the working electrode (WE) it might lead to a lower CE compared to Pt which has the ability to limit the reaction between deposited lithium and the

surrounding electrolyte more effectively. In this study Pt was not used as the WE due to its tendency to form a range of alloys, while Ni is largely inert (Yoon et al., 2015; Pal et al., 2020).

The 20 mol% $LiBF_4$/$[C_2moxa][BF_4]$ electrolyte initially exhibited a CE of 26% during the first cycle. Subsequently, the CE gradually increased and reached 35% by the fifth cycle. Also, two distinct cathodic peaks were initially observed at −1.6 V and −2.8 V vs. Fc/Fc^+. Prior research examining the impact of residual water and oxygen indicated that dissolved oxygen reduces around 2 V, with trace water reduction occurring within the 1.0–1.5 V range (Moshkovich et al., 2001; Xu et al., 2006). However, it is worth noting that these values may vary depending on factors like the choice of the working electrode and other experimental conditions. We propose that the −1.6 V cathodic peak is likely related to trace water or oxygen within the electrolyte, near the Ni electrode. Notably, its current density increased from the first to the second cycle but then declined. This suggests that during the initial cycle, formation of the SEI inhibits the reduction of trace impurities or that any trace water/oxygen had been depleted. The second cathodic peak at −2.8 V *versus* Fc/Fc^+ is attributed to SEI formation by reduction of the 20 mol% $LiBF_4$/$[C_2moxa][BF_4]$ electrolyte. Although the CV of the electrochemical window of neat $[C_2moxa][BF_4]$ in acetonitrile demonstrated cathodic stability up to −3.2 V (Figures 7), the addition of $LiBF_4$ and use of the Ni electrode rather than Pt may have decreased the reductive stability.

In the 20 mol% $LiBF_4$ system, a crossover of the current is noted at −3.8 V for all cycles. This phenomenon has also been reported in electrolytes such as $[C_3mpyr][FSI]$/0.2 mol kg^{-1} LiFSI and $[C_3mpyr][FSI]$/0.45 mol kg^{-1} LiFSI (WE= Ni, 50 mV s^{-1}, 22°C) (Bhatt et al., 2010), with observations of the crossover currents at −3.7 V and −3.6 V respectively. According to previous findings, this crossover current suggests that the electroplating of Li onto the Ni electrode requires an overpotential to initiate nucleation and subsequent Li growth (Xu et al., 2006). This behavior was also noticed in the 50 mol% $LiBF_4$/$[C_2moxa][BF_4]$ at −2.9 V and 50 mol % LiFSI/$[C_2moxa][BF_4]$ at −3.3 V. Lithium plating/stripping measurements were conducted for the 50 mol% $LiBF_4$ in $[C_2moxa][BF_4]$ system at both room temperature (Supplementary Figure S3) and 50°C (Figures 8D). In agreement with other systems, the cathodic and anodic current showed a consistent decrease with the cycle number, indicating the formation of a passivation layer. The 50 mol% $LiBF_4$ system exhibited a coulombic efficiency which fluctuates around 29%–22% for all 10 cycles (Supplementary Table S8).

The different current densities observed during lithium stripping/plating across all four electrolytes are likely a result of the different physical states of these liquid and quasi-solid electrolytes, and by the Li^+ concentration, which impact the mass transport properties, with the highest current observed in the high salt content liquid electrolyte.

6 Conclusion

A family of novel organic salts have been synthesised by pairing the *N*-ethyl-*N*-methyloxazolidinium cation $[C_2moxa]^+$ with a range of anions known for their potential applications in lithium battery electrolytes and the thermal properties, ion dynamics, structural and electrochemical properties characterised. The DSC analysis showed that $[C_2moxa][BF_4]$, $[C_2moxa][TFSI]$, and $[C_2moxa][PF_6]$ can be categorized as OIPCs while $[C_2moxa][FTFSI]$ is a room temperature ionic liquid. All three OIPCs showed at least one solid-solid phase transition. The $[C_2moxa][BF_4]$ displays the lowest ΔS_f (7 J mol^{-1} K^{-1}), indicating a very disordered phase I. $[C_2moxa][TFSI]$ was found to be a low melting solid (T_m= 51°C). The $[C_2moxa][PF_6]$ salt stands out for the large entropy phase II-I transition ($\Delta S_{II\text{-}I}$ = 42 J mol^{-1} K^{-1}), which promotes a disordered phase I and aligns with its high conductivity. The oxygen group on the cation lowers the melting points in all salts compared to those with non-ether counterparts like $[C_2mpyr]^+$ with similar anions. Adding an oxygen atom to the cation ring reduced T_{dec} values compared to pyrrolidinium counterparts, although all salts still displayed good thermal stability: the highest T_{dec} was observed for $[C_2moxa][TFSI]$ (369°C) and the lowest T_{dec} for the $[C_2moxa][FTFSI]$ IL (284°C).

The $[C_2moxa][BF_4]$ exhibits the highest solid-state ionic conductivity (8×10^{-6} S cm^{-1} at 30°C), with $[C_2moxa][PF_6]$ second highest at 6×10^{-6} S cm^{-1} at 30°C. The static solid state NMR spectra for $[C_2moxa][BF_4]$ and $[C_2moxa][PF_6]$ supported this by revealing faster dynamics for both cation and anion compared to the $[C_2moxa][TFSI]$ salt. The ionic conductivity of the $[C_2moxa][BF_4]$ salt (8×10^{-6} S cm^{-1} at 30°C) slightly exceeds that of $[C_2moxa][FSI]$ (4×10^{-6} S cm^{-1} at 30°C). Furthermore, $[C_2moxa]^+$ salts demonstrate high ionic conductivities compared to $[C_1moxa]^+$ salts and non-ether counterparts (with the pyrrolidinium cation), highlighting the favorable influence of both the ethyl side chain and the cyclic ether cation on the transport properties. In addition, the widest EW was reported for $[C_2moxa][BF_4]$ (4.8 V) and $[C_2moxa][TFSI]$ (4.1 V) while both $[C_2moxa][PF_6]$ and $[C_2moxa][TFSI]$ exhibited an EW of 3.7 V.

The $[C_2moxa][BF_4]$ and $[C_2moxa][FSI]$ salts were further used to prepare electrolyte mixtures with lithium salts (10, 20 and 50 mol %) of the same anion. The electrolytes composed of 50 mol% $LiBF_4$ and 10 mol% LiFSI became quasi-solids, while the other electrolyte mixtures were liquids at 30°C.

The highest conductivity of 2×10^{-3} S cm^{-1} at 30°C was found for the 20 mol% LiFSI/$[C_2moxa][FSI]$ electrolyte. The 50 mol% $LiBF_4$/$[C_2moxa][BF_4]$ showed the lowest conductivity, of 3×10^{-5} S cm^{-1} at 30°C. The $LiBF_4$/$[C_2moxa][BF_4]$ mixtures exhibited lower conductivities compared to LiFSI/$[C_2moxa][FSI]$ mixtures, which was consistent with the diffusion coefficients measured by PFG NMR. The diffusivity values for all ions (D_{H^+}, D_{F^-}, and D_{Li^+}) in the $[C_2moxa][FSI]$ electrolyte mixtures (in the range of 10^{-11} m^2 s^{-1}) were higher than in the $[C_2moxa][BF_4]$ electrolytes (in the range of 10^{-12}–10^{-13} m^2 s^{-1}) at all temperatures. In both LiFSI and $LiBF_4$ mixtures, the 20 mol% system showed higher conductivity compared to the 10 mol% systems.

Finally, preliminary lithium plating/stripping experiments and initial coulombic efficiency measurements show all four $[C_2moxa]^+$ electrolytes support stable lithium cycling. The 50 and 20 mol% LiFSI in $[C_2moxa][FSI]$ systems demonstrated distinct plating and stripping peaks and stable CE compared to the $[C_2moxa][BF_4]$ electrolytes. The 20 mol% LiFSI/$[C_2moxa][FSI]$ electrolyte exhibited the highest CE among all the systems studied, with a 53%–47% efficiency over 10 cycles. Thus, this study presents a novel family of oxazolidinium salts that exhibit promising characteristics

for use as ionic electrolytes, offering insights to enhance electrolyte properties and performance, particularly for lithium metal batteries.

Data availability statement

The original contributions presented in the study are included in the article/Supplementary Material, further inquiries can be directed to the corresponding author.

Author contributions

AS: Formal Analysis, Writing–original draft, Writing–review and editing. CK: Writing–review and editing. FF: Investigation, Supervision, Writing–review and editing. OH: Resources, Writing–review and editing. LO: Supervision, Writing–review and editing. JP: Conceptualization, Investigation, Supervision, Writing–review and editing.

Funding

The author(s) declare financial support was received for the research, authorship, and/or publication of this article. This work was supported by funding from the Australian Research Council (ARC) through the ARC Industrial Transformation Training Centre for Future Energy Storage Technologies IC180100049 (storEnergy) and Discovery Project DP210101269.

Conflict of interest

The authors declare that the research was conducted in the absence of any commercial or financial relationships that could be construed as a potential conflict of interest.

Publisher's note

All claims expressed in this article are solely those of the authors and do not necessarily represent those of their affiliated organizations, or those of the publisher, the editors and the reviewers. Any product that may be evaluated in this article, or claim that may be made by its manufacturer, is not guaranteed or endorsed by the publisher.

Supplementary material

The Supplementary Material for this article can be found online at: https://www.frontiersin.org/articles/10.3389/fbael.2024.1330604/full#supplementary-material

References

Abeysooriya, S., Lee, M., O'Dell, L. A., and Pringle, J. M. (2022). Plastic crystal-based electrolytes using novel dicationic salts. *Phys. Chem. Chem. Phys.* 24, 4899–4909. doi:10.1039/d1cp04314e

Abu-Lebdeh, Y., Abouimrane, A., Alarco, P. J., and Armand, M. (2006). Ionic liquid and plastic crystalline phases of pyrazolium imide salts as electrolytes for rechargeable lithium-ion batteries. *J. Power Sources* 154, 255–261. doi:10.1016/j.jpowsour.2005.03.231

Al-Masri, D., Yunis, R., Hollenkamp, A. F., Doherty, C. M., and Pringle, J. M. (2020a). The influence of alkyl chain branching on the properties of pyrrolidinium-based ionic electrolytes. *Phys. Chem. Chem. Phys.* 22, 18102–18113. doi:10.1039/d0cp03046e

Al-Masri, D., Yunis, R., Hollenkamp, A. F., and Pringle, J. M. (2018). A symmetrical ionic liquid/Li salt system for rapid ion transport and stable lithium electrochemistry. *Chem. Commun.* 54, 3660–3663. doi:10.1039/c8cc00531a

Al-Masri, D., Yunis, R., Hollenkamp, A. F., and Pringle, J. M. (2020b). Designing solid-state electrolytes through the structural modification of a high-performing ionic liquid. *ChemElectroChem* 7, 4118–4123. doi:10.1002/celc.202000772

Appetecchi, G. B., Montanino, M., Carewska, M., Moreno, M., Alessandrini, F., and Passerini, S. (2011). Chemical–physical properties of bis(perfluoroalkylsulfonyl)imide-based ionic liquids. *Electrochimica Acta* 56, 1300–1307. doi:10.1016/j.electacta.2010.10.023

Armel, V., Velayutham, D., Sun, J., Howlett, P. C., Forsyth, M., MacFarlane, D. R., et al. (2011). Ionic liquids and organic ionic plastic crystals utilizing small phosphonium cations. *J. Mater Chem.* 21, 7640–7650. doi:10.1039/c1jm10417a

Basile, A., Bhatt, A. I., and O'Mullane, A. P. (2016). Anion effect on lithium electrodeposition from N-propyl- N-methylpyrrolidinium bis(fluorosulfonyl)imide ionic liquid electrolytes. *Electrochimica Acta* 215, 19–28. doi:10.1016/j.electacta.2016.08.075

Bayley, P. M., Best, A. S., MacFarlane, D. R., and Forsyth, M. (2011). Transport properties and phase behaviour in binary and ternary ionic liquid electrolyte systems of interest in lithium batteries. *ChemPhysChem* 12, 823–827. doi:10.1002/cphc.201000909

Bhatt, A. I., Best, A. S., Huang, J., and Hollenkamp, A. F. (2010). Application of the N-propyl-N-methyl-pyrrolidinium bis(fluorosulfonyl)imide RTIL containing lithium bis(fluorosulfonyl)imide in ionic liquid based lithium batteries. *J. Electrochem Soc.* 157, 66–74. doi:10.1149/1.3257978

Biernacka, K., Al-Masri, D., Yunis, R., Zhu, H., Hollenkamp, A. F., and Pringle, J. M. (2020). Development of new solid-state electrolytes based on a hexamethylguanidinium plastic crystal and lithium salts. *Electrochimica Acta* 357, 136863. doi:10.1016/j.electacta.2020.136863

Biernacka, K., Makhlooghiazad, F., Popov, I., Zhu, H., Chotard, J. N., Forsyth, C. M., et al. (2021). Investigation of unusual conductivity behavior and ion dynamics in hexamethylguanidinium bis(fluorosulfonyl)imide-based electrolytes for sodium batteries. *J. Phys. Chem. C* 125, 12518–12530. doi:10.1021/acs.jpcc.1c01777

Cha, J. H., Kim, K. S., Choi, S., Yeon, S. H., Lee, H., Kim, H. S., et al. (2005). Thermal and electrochemical properties of morpholinium salts with bromide anion. *Korean J. Chem. Eng.* 22, 945–948. doi:10.1007/bf02705680

Chen, F., and Forsyth, M. (2019). Computational investigation of mixed anion effect on lithium coordination and transport in salt concentrated ionic liquid electrolytes. *J. Phys. Chem. Lett.* 10, 7414–7420. doi:10.1021/acs.jpclett.9b02416

Choi, S., Kim, K.-S., Lee, H., Oh, J. S., and Lee, B.-B. (2005). Synthesis and ionic conductivities of lithium-doped morpholinium salts. *Korean J. Chem. Eng.* 22, 281–284. doi:10.1007/bf02701498

Diallo, A. O., Morgan, A. B., Len, C., and Marlair, G. (2013). An innovative experimental approach aiming to understand and quantify the actual fire hazards of ionic liquids. *Energy Environ. Sci.* 6, 699–710. doi:10.1039/c2ee23926d

Eshetu, G. G., Jeong, S., Pandard, P., Lecocq, A., Marlair, G., and Passerini, S. (2017). Comprehensive insights into the thermal stability, biodegradability, and combustion chemistry of pyrrolidinium-based ionic liquids. *ChemSusChem* 10, 3146–3159. doi:10.1002/cssc.201701006

Fan, L., Wei, S., Li, S., Li, Q., and Lu, Y. (2018). Recent progress of the solid-state electrolytes for high-energy metal-based batteries. *Adv. Energy Mater.* 8, 1–31. doi:10.1002/aenm.201702657

Fang, S., Yang, L., Wang, J., Li, M., Tachibana, K., and Kamijima, K. (2009). Ionic liquids based on functionalized guanidinium cations and TFSI anion as potential electrolytes. *Electrochimica Acta* 54, 4269–4273. doi:10.1016/j.electacta.2009.02.082

Fang, S., Zhang, Z., Jin, Y., Yang, L., Hirano, S. I., Tachibana, K., et al. (2011). New functionalized ionic liquids based on pyrrolidinium and piperidinium cations with two ether groups as electrolytes for lithium battery. *J. Power Sources* 196, 5637–5644. doi:10.1016/j.jpowsour.2011.02.047

Ferrari, S., Quartarone, E., Mustarelli, P., Magistris, A., Protti, S., Lazzaroni, S., et al. (2009). A binary ionic liquid system composed of N-methoxyethyl-N-methylpyrrolidinium bis(trifluoromethanesulfonyl)-imide and lithium bis(trifluoromethanesulfonyl)imide: a new promising electrolyte for lithium batteries. *J. Power Sources* 194, 45–50. doi:10.1016/j.jpowsour.2008.12.013

Forsyth, M., Chimdi, T., Seeber, A., Gunzelmann, D., and Howlett, P. C. (2014). Structure and dynamics in an organic ionic plastic crystal, N-ethyl-N-methyl

pyrrolidinium bis(trifluoromethanesulfonyl) amide, mixed with a sodium salt. *J. Mater. Chem. A* 2, 3993–4003. doi:10.1039/c3ta15153k

Forsyth, S., Golding, J., Macfarlane, D. R., and Forsyth, M. (2001). N-methyl-N-alkylpyrrolidinium tetrafluoroborate salts: ionic solvents and solid electrolytes. *Electrochimica Acta* 46, 1753–1757. doi:10.1016/s0013-4686(00)00781-7

Galiński, M., Lewandowski, A., and Stepniak, I. (2006). Ionic liquids as electrolytes. *Electrochimica Acta* 51, 5567–5580. doi:10.1016/j.electacta.2006.03.016

García, Y., and O'Dell, L. A. (2022). Understanding the interfacial region in organic ionic plastic crystal composite electrolyte materials by solid-state NMR. *Curr. Opin. Colloid and Interface Sci.* 61, 101632. doi:10.1016/j.cocis.2022.101632

Girard, G. M. A., Hilder, M., Zhu, H., Nucciarone, D., Whitbread, K., Zavorine, S., et al. (2015). Electrochemical and physicochemical properties of small phosphonium cation ionic liquid electrolytes with high lithium salt content. *Phys. Chem. Chem. Phys.* 17, 8706–8713. doi:10.1039/c5cp00205b

Golding, J., Hamid, N., MacFarlane, D. R., Forsyth, M., Forsyth, C., Collins, C., et al. (2001). *N*-Methyl-*N*-alkylpyrrolidinium hexafluorophosphate Salts: novel molten salts and plastic crystal phases. *Chem. Mater* 13, 558–564. doi:10.1021/cm000625w

Han, Y., Liu, B., Xiao, Z., Zhang, W., Wang, X., Pan, G., et al. (2021). Interface issues of lithium metal anode for high-energy batteries: challenges, strategies, and perspectives. *InfoMat* 3, 155–174. doi:10.1002/inf2.12166

Hatzell, K. B., Chen, X. C., Cobb, C. L., Dasgupta, N. P., Dixit, M. B., Marbella, L. E., et al. (2020). Challenges in lithium metal anodes for solid-state batteries. *ACS Energy Lett.* 5, 922–934. doi:10.1021/acsenergylett.9b02668

Hill, A. J., Huang, J., Efthimiadis, J., Meakin, P., Forsyth, M., and Macfarlane, D. R. (2002). Microstructural and molecular level characterisation of plastic crystal phases of pyrrolidinium trifluoromethanesulfonyl salts. *Solid State Ionics* 154-155, 119–124. doi:10.1016/s0167-2738(02)00472-1

Howlett, P. C., Shekibi, Y., MacFarlane, D. R., and Forsyth, M. (2009). Li-Metal symmetrical cell studies using ionic organic plastic crystal electrolyte. *Adv. Eng. Mater* 11, 1044–1048. doi:10.1002/adem.200900186

Hu, F., and Song, T. (2017). Application of functionalized ether in lithium ion batteries. *RSC Adv.* 7, 54203–54212. doi:10.1039/c7ra11023e

Huo, S., Sheng, L., Xue, W., Wang, L., Xu, H., Zhang, H., et al. (2023). Challenges of polymer electrolyte with wide electrochemical window for high energy solid-state lithium batteries. *InfoMat* 5, 1–32. doi:10.1002/inf2.12394

Iranipour, N., Gunzelmann, D. J., Seeber, A. J., Vongsvivut, J., Hollenkamp, A. F., Forsyth, M., et al. (2017). Effect of secondary phase on thermal behaviour and solid-state ion conduction in lithium doped *N*-ethyl-*N*-methylpyrrolidinium tetrafluoroborate organic ionic plastic crystal. *J. Mater. Chem. A* 5, 24909–24919. doi:10.1039/c7ta08653a

Janikowski, J., Forsyth, C., MacFarlane, D. R., and Pringle, J. M. (2011). Novel ionic liquids and plastic crystals utilizing the cyanate anion. *J. Mater Chem.* 21, 19219–19225. doi:10.1039/c1jm14055h

Jeong, S., Li, S., Appetecchi, G. B., and Passerini, S. (2019). Asymmetric ammonium-based ionic liquids as electrolyte components for safer, high-energy, electrochemical storage devices. *Energy Storage Mater.* 18, 1–9. doi:10.1016/j.ensm.2019.01.015

Jin, L., Howlett, P. C., Pringle, J. M., Janikowski, J., Armand, M., MacFarlane, D. R., et al. (2014). An organic ionic plastic crystal electrolyte for rate capability and stability of ambient temperature lithium batteries. *Energy Environ. Sci.* 7, 3352–3361. doi:10.1039/c4ee01085j

Jin, L., Nairn, K. M., Forsyth, C. M., Seeber, A. J., MacFarlane, D. R., Howlett, P. C., et al. (2012). Structure and transport properties of a plastic crystal ion conductor: diethyl(methyl)(isobutyl)phosphonium hexafluorophosphate. *J. Am. Chem. Soc.* 134, 9688–9697. doi:10.1021/ja301175v

Jin, L., Nairn, K. M., Ling, C. D., Zhu, H., O'Dell, L. A., Li, J., et al. (2017). Conformational dynamics in an organic ionic plastic crystal. *J. Phys. Chem. B* 121, 5439–5446. doi:10.1021/acs.jpcb.7b02780

Kang, C. S. M., Hutt, O. E., and Pringle, J. M. (2022). Halide-free synthesis of new difluoro(oxalato)borate $[DFOB]^-$-Based ionic liquids and organic ionic plastic crystals. *ChemPhysChem* 23, e202200115. doi:10.1002/cphc.202200115

Kang, C. S. M., Yunis, R., Zhu, H., Doherty, C. M., Hutt, O. E., and Pringle, J. M. (2021). Ionic liquids and plastic crystals utilising the oxazolidinium cation: the effect of ether functionality in the ring. *Mater Chem. Front.* 5, 6014–6026. doi:10.1039/d1qm00648g

Kerner, M., Plylahan, N., Scheers, J., and Johansson, P. (2015). *Phys. Chem. Chem. Phys.* 17, 19569–19581. doi:10.1039/c5cp01891a

Kim, K. S., Choi, S., Demberelnyamba, D., Lee, H., Oh, J., Lee, B. B., et al. (2004). Ionic liquids based on N-alkyl-N-methylmorpholinium salts as potential electrolytes. *Chem. Commun.* 10, 828–829. doi:10.1039/b400198b

Kunze, M., Jeong, S., Paillard, E., Winter, M., and Passerini, S. (2010a). Melting behavior of pyrrolidinium-based ionic liquids and their binary mixtures. *J. Phys. Chem. C* 114, 12364–12369. doi:10.1021/jp103746k

Kunze, M., Montanino, M., Appetecchi, G. B., Jeong, S., Schönhoff, M., Winter, M., et al. (2010b). Melting behavior and ionic conductivity in hydrophobic ionic liquids. *J. Phys. Chem. A* 114, 1776–1782. doi:10.1021/jp9099418

Lane, G. H. (2012). Electrochemical reduction mechanisms and stabilities of some cation types used in ionic liquids and other organic salts. *Electrochimica Acta* 83, 513–528. doi:10.1016/j.electacta.2012.08.046

Lane, G. H., Bayley, P. M., Clare, B. R., Best, A. S., MacFarlane, D. R., Forsyth, M., et al. (2010). Ionic liquid electrolyte for lithium metal batteries: physical, electrochemical, and interfacial studies of *N*-methyl-*N*-butylmorpholinium bis(fluorosulfonyl)imide. *J. Phys. Chem. C* 114, 21775–21785. doi:10.1021/jp1054809

Lee, M., Lee, Y. H., Park, J. H., and Choi, U. H. (2017). Bis-imidazolium iodide organic ionic plastic crystals and their applications to solid state dye-sensitized solar cells. *Org. Electron.* 48, 241–247. doi:10.1016/j.orgel.2017.06.004

Lethesh, K. C., Bahaa, A., Abdullah, M., Bamgbopa, M. O., and Susantyoko, R. A. (2022). Temperature-dependent electrochemical stability window of bis(trifluoromethanesulfonyl)imide and bis(fluorosulfonyl)imide anion based ionic liquids. *Front. Chem.* 10, 859304–859314. doi:10.3389/fchem.2022.859304

Liu, Y., Lin, D., Yuen, P. Y., Liu, K., Xie, J., Dauskardt, R. H., et al. (2017). An artificial solid electrolyte interphase with high Li-ion conductivity, mechanical strength, and flexibility for stable lithium metal anodes. *Adv. Mater.* 29, 1–8. doi:10.1002/adma.201605531

Macfarlane, D. R., and Forsyth, M. (2001). Plastic crystal electrolyte materials: new perspectives on solid state ionics. *Adv. Mater* 13, 12–13.

MacFarlane, D. R., Meakin, P., Amini, N., and Forsyth, M. (2001). Structural studies of ambient temperature plastic crystal ion conductors. *J. Phys. Condens. Matter* 13, 8256–8267. doi:10.1088/0953-8984/13/36/303

MacFarlane, D. R., Meakin, P., Sun, J., Amini, N., and Forsyth, M. (1999). Pyrrolidinium Imides: A new family of molten salts and conductive plastic crystal phases. *J. Phys. Chem. B* 103, 4164–4170. doi:10.1021/jp984145s

Makhlooghiazad, F., Yunis, R., Mecerreyes, D., Armand, M., Howlett, P. C., and Forsyth, M. (2017). Comparison of the physicochemical and electrochemical behaviour of mixed anion phosphonium based OIPCs electrolytes for sodium batteries. *Solid State Ionics* 312, 44–52. doi:10.1016/j.ssi.2017.10.014

Martin, P. A., Chen, F., Forsyth, M., Deschamps, M., and O'Dell, L. A. (2018). Correlating intermolecular cross-relaxation rates with distances and coordination numbers in ionic liquids. *J. Phys. Chem. Lett.* 9, 7072–7078. doi:10.1021/acs.jpclett.8b03021

Martinelli, A., Matic, A., Jacobsson, P., Börjesson, L., Fernicola, A., and Scrosati, B. (2009). Phase behavior and ionic conductivity in lithium bis(trifluoromethanesulfonyl) imide-doped ionic liquids of the pyrrolidinium cation and bis(trifluoromethanesulfonyl)imide anion. *J. Phys. Chem. B* 113, 11247–11251. doi:10.1021/jp905783t

Matsumoto, H., Sakaebe, H., and Tatsumi, K. (2005). Preparation of room temperature ionic liquids based on aliphatic onium cations and asymmetric amide anions and their electrochemical properties as a lithium battery electrolyte. *J. Power Sources* 146, 45–50. doi:10.1016/j.jpowsour.2005.03.103

Matsumoto, H., Sakaebe, H., Tatsumi, K., Kikuta, M., Ishiko, E., and Kono, M. (2006). Fast cycling of Li/LiCoO2 cell with low-viscosity ionic liquids based on bis(fluorosulfonyl)imide [FSI]−. *J. Power Sources* 160, 1308–1313. doi:10.1016/j.jpowsour.2006.02.018

Matsumoto, K., Harinaga, U., Tanaka, R., Koyama, A., Hagiwara, R., and Tsunashima, K. (2014). The structural classification of the highly disordered crystal phases of $[N_n][BF_4]$, $[N_n][PF_6]$, $[P_n][BF_4]$, and $[P_n][PF_6]$ salts (N_n^+= tetraalkylammonium and P_n^+= tetraalkylphosphonium). *Phys. Chem. Chem. Phys.* 16, 23616–23626. doi:10.1039/c4cp03391d

Montanino, M., Moreno, M., Alessandrini, F., Appetecchi, G. B., Passerini, S., Zhou, Q., et al. (2012). Physical and electrochemical properties of binary ionic liquid mixtures: (1−x) PYR14TFSI−(x) PYR14IM14. *Electrochimica Acta* 60, 163–169. doi:10.1016/j.electacta.2011.11.030

Moshkovich, M., Gofer, Y., and Aurbach, D. (2001). Investigation of the electrochemical windows of aprotic alkali metal (Li, Na, K) salt solutions. *J. Electrochem Soc.* 148, 155–167. doi:10.1149/1.1357316

Navarra, M. A., Fujimura, K., Sgambetterra, M., Tsurumaki, A., Panero, S., Nakamura, N., et al. (2017). New ether-functionalized morpholinium- and piperidinium-based ionic liquids as electrolyte components in lithium and lithium–ion batteries. *ChemSusChem* 10, 2496–2504. doi:10.1002/cssc.201700346

Nti, F., Greene, G. W., Zhu, H., Howlett, P. C., Forsyth, M., and Wang, X. (2021). Anion effects on the properties of OIPC/PVDF composites. *Mater Adv.* 2, 1683–1694. doi:10.1039/d0ma00992j

Pal, U., Chen, F., Gyabang, D., Pathirana, T., Roy, B., Kerr, R., et al. (2020). Enhanced ion transport in an ether aided super concentrated ionic liquid electrolyte for long-life practical lithium metal battery applications. *J. Mater. Chem. A* 8, 18826–18839. doi:10.1039/d0ta06344d

Passerini, S., and Appetecchi, G. B. (2013). Toward more environmentally friendly routes to high purity ionic liquids. *MRS Bull.* 38, 540–547. doi:10.1557/mrs.2013.155

Plechkova, N. V., and Seddon, K. R. (2008). Applications of ionic liquids in the chemical industry. *Chem. Soc. Rev.* 37, 123–150. doi:10.1039/b006677j

Popov, I., Biernacka, K., Zhu, H., Nti, F., Porcarelli, L., Wang, X., et al. (2020). Strongly correlated ion dynamics in plastic ionic crystals and polymerized ionic liquids. *J. Phys. Chem. C* 124, 17889–17896. doi:10.1021/acs.jpcc.0c03297

Ramesh, S., Liew, C. W., and Ramesh, K. (2011). Evaluation and investigation on the effect of ionic liquid onto PMMA-PVC gel polymer blend electrolytes. *J. Non-Crystalline Solids* 357, 2132–2138. doi:10.1016/j.jnoncrysol.2011.03.004

Reiter, J., Jeremias, S., Paillard, E., Winter, M., and Passerini, S. (2013). Fluorosulfonyl-(trifluoromethanesulfonyl)imide ionic liquids with enhanced asymmetry. *Phys. Chem. Chem. Phys.* 15, 2565–2571. doi:10.1039/c2cp43066e

Scrosati, B., Hassoun, J., and Sun, Y. K. (2011). Lithium-ion batteries. A look into the future. *Energy Environ. Sci.* 4, 3287–3295. doi:10.1039/c1ee01388b

Shekibi, Y., Rüther, T., Huang, J., and Hollenkamp, A. F. (2012). Realisation of an all solid state lithium battery using solid high temperature plastic crystal electrolytes exhibiting liquid like conductivity. *Phys. Chem. Chem. Phys.* 14, 4597–4604. doi:10.1039/c2cp24077g

Shi, Z., Liu, M., Naik, D., and Gole, J. L. (2001). Electrochemical properties of Li–Mg alloy electrodes for lithium batteries. *J. Power Sources* 92, 70–80. doi:10.1016/s0378-7753(00)00521-8

Shimizu, M., Yamaguchi, K., Usui, H., Ieuji, N., Yamashita, T., Komura, T., et al. (2020). Piperidinium-based ionic liquids as an electrolyte solvent for Li-ion batteries: effect of number and position of oxygen atom in cation side chain on electrolyte property. *J. Electrochem Soc.* 167, 070516. doi:10.1149/1945-7111/ab6a89

Smiglak, M., Reichert, W. M., Holbrey, J. D., Wilkes, J. S., Sun, L., Thrasher, J. S., et al. (2006). *Chem. Commun.* 24, 2554–2556. doi:10.1039/b602086k

Stachurski, C. D., Davis, J. H., Cosby, T., Crowley, M. E., Larm, N. E., Ballentine, M. G., et al. (2023). Physical and electrochemical analysis of *N*-Alkylpyrrolidinium-Substituted boronium ionic liquids. *Inorg. Chem.* 62, 18280–18289. doi:10.1021/acs.inorgchem.3c02971

Theivaprakasam, S., MacFarlane, D. R., and Mitra, S. (2015). Electrochemical studies of N-Methyl N-Propyl Pyrrolidinium bis(trifluoromethanesulfonyl) imide ionic liquid mixtures with conventional electrolytes in LiFePO4/Li cells. *Electrochimica Acta* 180, 737–745. doi:10.1016/j.electacta.2015.08.137

Thomas, M. L., Hatakeyama-Sato, K., Nanbu, S., and Yoshizawa-Fujita, M. (2023). Organic ionic plastic crystals: flexible solid electrolytes for lithium secondary batteries. *Energy Adv.* 2, 748–764. doi:10.1039/d3ya00078h

Tian, S., Shao, B., Wang, Z., Li, S., Liu, X., Zhao, Y., et al. (2019). Organic ionic plastic crystal as electrolyte for lithium-oxygen batteries. *Chin. Chem. Lett.* 30, 1289–1292. doi:10.1016/j.cclet.2019.02.027

Timmermans, J. (1961). Preface. *J. Phys. Chem. Solids* 18, 8. doi:10.1016/0022-3697(61)90075-0

Wang, L., and Xia, C. (2011). Theory study on structure property of N-ethyl morpholinium ionic liquid of different alkyl length. *Adv. Mater. Res.* 301–303, 170–174. doi:10.4028/www.scientific.net/amr.301-303.170

Warrington, A., Kang, C. S. M., Forsyth, C., Doherty, C. M., Acharya, D., O'Dell, L. A., et al. (2022). Thermal, structural and dynamic properties of ionic liquids and organic ionic plastic crystals with a small ether-functionalised cation. *Mater Chem. Front.* 6, 1437–1455. doi:10.1039/d2qm00045h

Wei, Z., Ren, Y., Wang, M., He, J., Huo, W., and Tang, H. (2020). Improving the conductivity of solid polymer electrolyte by grain reforming. *Nanoscale Res. Lett.* 15, 1–8. doi:10.1186/s11671-020-03355-4

Wibowo, R., Ward Jones, S. E., and Compton, R. G. (2009). Kinetic and thermodynamic parameters of the Li/Li^+ couple in the room temperature ionic liquid *N*-butyl-*N*-methylpyrrolidinium bis(trifluoromethylsulfonyl) imide in the temperature range 298–318 K: A theoretical and experimental study using Pt and Ni electrodes. *J. Phys. Chem. B* 113, 12293–12298. doi:10.1021/jp906128t

Wooster, T. J., Johanson, K. M., Fraser, K. J., MacFarlane, D. R., and Scott, J. L. (2006). Thermal degradation of cyano containing ionic liquids. *Green Chem.* 8, 691. doi:10.1039/b606395k

Wu, L., Venkatanarayananan, R. I., Shi, X., Roy, D., and Krishnan, S. (2014). Glass transition, viscosity, and conductivity correlations in solutions of lithium salts in PEGylated imidazolium ionic liquids. *J. Mol. Liq.* 198, 398–408. doi:10.1016/j.molliq.2014.07.031

Xu, J., Yang, J., NuLi, Y., Wang, J., and Zhang, Z. (2006). Additive-containing ionic liquid electrolytes for secondary lithium battery. *J. Power Sources* 160, 621–626. doi:10.1016/j.jpowsour.2006.01.054

Yamada, H., Miyachi, Y., Takeoka, Y., Rikukawa, M., and Yoshizawa-Fujita, M. (2019). Pyrrolidinium-based organic ionic plastic crystals: relationship between side chain length and properties. *Electrochimica Acta* 303, 293–298. doi:10.1016/j.electacta.2019.02.076

Yamaguchi, S., Yamada, H., Takeoka, Y., Rikukawa, M., and Yoshizawa-Fujita, M. (2019). Synthesis of pyrrolidinium-based plastic crystals exhibiting high ionic conductivity at ambient temperature. *New J. Chem.* 43, 4008–4012. doi:10.1039/c8nj05127e

Yang, K., Zhang, Z., Liao, Z., Yang, L., and Hirano, S. (2018). Organic ionic plastic crystal-polymer solid electrolytes with high ionic conductivity and mechanical ability for solid-state lithium ion batteries. *ChemistrySelect* 3, 12595–12599. doi:10.1002/slct.201803094

Yeon, S. H., Kim, K. S., Choi, S., Lee, H., Kim, H. S., and Kim, H. (2005). Physical and electrochemical properties of 1-(2-hydroxyethyl)-3-methyl imidazolium and N-(2-hydroxyethyl)-N-methyl morpholinium ionic liquids. *Electrochimica Acta* 50, 5399–5407. doi:10.1016/j.electacta.2005.03.020

Yoon, H., Best, A. S., Forsyth, M., MacFarlane, D. R., and Howlett, P. C. (2015). Physical properties of high Li-ion content N-propyl-N-methylpyrrolidinium bis(fluorosulfonyl)imide based ionic liquid electrolytes. *Phys. Chem. Chem. Phys.* 17, 4656–4663. doi:10.1039/c4cp05333h

Yoon, H., Lane, G. H., Shekibi, Y., Howlett, P. C., Forsyth, M., Best, A. S., et al. (2013). Lithium electrochemistry and cycling behaviour of ionic liquids using cyano based anions. *Energy Environ. Sci.* 6, 979–986. doi:10.1039/c3ee23753b

Yunis, R., Al-Masri, D., Hollenkamp, A. F., Doherty, C. M., Zhu, H., and Pringle, J. M. (2020a). Plastic crystals utilising small ammonium cations and sulfonylimide anions as electrolytes for lithium batteries. *J. Electrochem. Soc.* 167, 070529. doi:10.1149/1945-7111/ab76a2

Yunis, R., Girard, G. M. A., Wang, X., Zhu, H., Bhattacharyya, A. J., Howlett, P., et al. (2018b). The anion effect in ternary electrolyte systems using poly(diallyldimethylammonium) and phosphonium-based ionic liquid with high lithium salt concentration. *Solid State Ionics* 327, 83–92. doi:10.1016/j.ssi.2018.10.018

Yunis, R., Hollenkamp, A. F., Forsyth, C., Doherty, C. M., Al-Masri, D., and Pringle, J. M. (2019). Organic salts utilising the hexamethylguanidinium cation: the influence of the anion on the structural, physical and thermal properties. *Phys. Chem. Chem. Phys.* 21, 12288–12300. doi:10.1039/c9cp01740b

Yunis, R., Newbegin, T. W., Hollenkamp, A. F., and Pringle, J. M. (2018a). Ionic liquids and plastic crystals with a symmetrical pyrrolidinium cation. *Mater Chem. Front.* 2, 1207–1214. doi:10.1039/c8qm00016f

Yunis, R., Pringle, J. M., Wang, X., Girard, G. M. A., Kerr, R., Zhu, H., et al. (2020b). Solid (cyanomethyl)trimethylammonium salts for electrochemically stable electrolytes for lithium metal batteries. *J. Mater. Chem. A* 8, 14721–14735. doi:10.1039/d0ta03502e

Zhou, Y., Wang, X., Zhu, H., Armand, M., Forsyth, M., Greene, G. W., et al. (2017a). N-ethyl-N-methylpyrrolidinium bis(fluorosulfonyl)imide-electrospun polyvinylidene fluoride composite electrolytes: characterization and lithium cell studies. *Phys. Chem. Chem. Phys.* 19, 2225–2234. doi:10.1039/c6cp07415d

Zhou, Y., Wang, X., Zhu, H., Armand, M., Forsyth, M., Greene, G. W., et al. (2018). Ternary lithium-salt organic ionic plastic crystal polymer composite electrolytes for high voltage, all-solid-state batteries. *Energy Storage Mater.* 15, 407–414. doi:10.1016/j.ensm.2018.07.017

Zhou, Y., Wang, X., Zhu, H., Yoshizawa-Fujita, M., Miyachi, Y., Armand, M., et al. (2017b). Solid-state lithium conductors for lithium metal batteries based on electrospun nanofiber/plastic crystal composites. *ChemSusChem* 10, 3135–3145. doi:10.1002/cssc.201700691

Zhou, Z., Matsumoto, H., and Tatsumi, K. (2005). Low-melting, low-viscous, hydrophobic ionic liquids: aliphatic quaternary ammonium salts with perfluoroalkyltrifluoroborates. *Chem. – A Eur. J.* 11, 752–766. doi:10.1002/chem.200400817

Zhou, Z., Matsumoto, H., and Tatsumi, K. (2006). Cyclic quaternary ammonium ionic liquids with perfluoroalkyltrifluoroborates: synthesis, characterization, and properties. *Chem. – A Eur. J.* 12, 2196–2212. doi:10.1002/chem.200500930

Zhou, Z. B., and Matsumoto, H. (2007). Lithium-doped, organic ionic plastic crystal electrolytes exhibiting high ambient-temperature conductivities. *Electrochem. Commun.* 9, 1017–1022. doi:10.1016/j.elecom.2006.12.012

Zhu, H., MacFarlane, D. R., Pringle, J. M., and Forsyth, M. (2019). Organic ionic plastic crystals as solid-state electrolytes. *Trends Chem.* 1, 126–140. doi:10.1016/j.trechm.2019.01.002

Zhu, H., and O'Dell, L. A. (2021). Nuclear magnetic resonance characterisation of ionic liquids and organic ionic plastic crystals: common approaches and recent advances. *Chem. Commun.* 57, 5609–5625. doi:10.1039/d1cc02151f

Zhu, H., Rana, U. A., Ranganathan, V., Jin, L., O'Dell, L. A., MacFarlane, D. R., et al. (2014). Proton transport behaviour and molecular dynamics in the guanidinium triflate solid and its mixtures with triflic acid. *J. Mater Chem. A Mater* 2, 681–691. doi:10.1039/c3ta13344c